On the Richtmyer–Meshkov instability evolving from a deterministic multimode planar interface

V. K. Tritschler[1,2,†], **B. J. Olson**[3], **S. K. Lele**[2], **S. Hickel**[1], **X. Y. Hu**[1] and **N. A. Adams**[1]

[1]Institute of Aerodynamics and Fluid Mechanics, Technische Universität München, 85747 Garching, Germany

[2]Department of Aeronautics and Astronautics, Stanford University, Stanford, CA 94305, USA

[3]Lawrence Livermore National Laboratory, Livermore, CA 94550, USA

We investigate the shock-induced turbulent mixing between a light and a heavy gas, where a Richtmyer–Meshkov instability (RMI) is initiated by a shock wave with Mach number $Ma = 1.5$. The prescribed initial conditions define a deterministic multimode interface perturbation between the gases, which can be imposed exactly for different simulation codes and resolutions to allow for quantitative comparison. Well-resolved large-eddy simulations are performed using two different and independently developed numerical methods with the objective of assessing turbulence structures, prediction uncertainties and convergence behaviour. The two numerical methods differ fundamentally with respect to the employed subgrid-scale regularisation, each representing state-of-the-art approaches to RMI. Unlike previous studies, the focus of the present investigation is to quantify the uncertainties introduced by the numerical method, as there is strong evidence that subgrid-scale regularisation and truncation errors may have a significant effect on the linear and nonlinear stages of the RMI evolution. Fourier diagnostics reveal that the larger energy-containing scales converge rapidly with increasing mesh resolution and thus are in excellent agreement for the two numerical methods. Spectra of gradient-dependent quantities, such as enstrophy and scalar dissipation rate, show stronger dependences on the small-scale flow field structures as a consequence of truncation error effects, which for one numerical method are dominantly dissipative and for the other dominantly dispersive. Additionally, the study reveals details of various stages of RMI, as the flow transitions from large-scale nonlinear entrainment to fully developed turbulent mixing. The growth rates of the mixing zone widths as obtained by the two numerical methods are $\sim t^{7/12}$ before re-shock and $\sim(t - t_0)^{2/7}$ long after re-shock. The decay rate of turbulence kinetic energy is consistently $\sim(t - t_0)^{-10/7}$ at late times, where the molecular mixing fraction approaches an asymptotic limit $\Theta \approx 0.85$. The anisotropy measure $\langle a \rangle_{xyz}$ approaches an asymptotic limit of ≈ 0.04, implying that no full recovery of isotropy within the mixing zone is obtained, even after re-shock. Spectra of density, turbulence kinetic energy, scalar dissipation rate and enstrophy are presented and show excellent agreement for the resolved scales. The probability density function of the heavy-gas mass fraction and vorticity reveal that the light–heavy gas composition within the mixing zone is accurately predicted, whereas it is more difficult to capture the long-term behaviour of the vorticity.

Key words: shock waves, turbulent mixing

† Email address for correspondence: volker.tritschler@aer.mw.tum.de

1. Introduction

The Richtmyer–Meshkov instability (Richtmyer 1960; Meshkov 1969) is a hydrodynamic instability that occurs at the interface separating two fluids of different densities. It shows similarities with the Rayleigh–Taylor instability (Rayleigh 1883; Taylor 1950), where initial perturbations at the interface grow and eventually evolve into a turbulent flow field through the transfer of potential to kinetic energy. In the limit of an impulsive acceleration of the interface, e.g. by a shock wave, the instability is referred to as a Richtmyer–Meshkov instability (RMI). In RMI, baroclinic vorticity production at the interface is caused by the misalignment of the pressure gradient (∇p) associated with the shock wave and the density gradient ($\nabla \rho$) of the material interface. The baroclinic vorticity production term $(\nabla \rho \times \nabla p)/\rho^2$ is the initial driving force of RMI. See Zabusky (1999) and Brouillette (2002) for comprehensive reviews.

RMI occurs on enormous scales in astrophysics (Arnett *et al.* 1989; Arnett 2000; Almgren *et al.* 2006), on intermediate scales in combustion (Yang, Kubota & Zukoski 1993; Khokhlov, Oran & Thomas 1999) and on very small scales in inertial confinement fusion (Lindl, McCrory & Campbell 1992; Taccetti *et al.* 2005; Aglitskiy *et al.* 2010). Owing to the fast time scales associated with RMI, laboratory experimental measurements have difficulties in characterising quantitatively initial perturbations of the material interface and capturing the evolution of the mixing zone. General insight into the flow physics of RMI relies to a considerable extent on numerical investigations, where large-eddy simulations (LES) have become an accepted tool during the past decade.

Hill, Pantano & Pullin (2006) performed a rigorous numerical investigation of RMI with re-shock. The authors used an improved version of the tuned centred difference–weighted essentially non-oscillatory (TCD-WENO) hybrid method of Hill & Pullin (2004). The method employs a switch to blend explicitly between a TCD stencil in smooth flow regions and a WENO shock-capturing stencil at discontinuities. The TCD-WENO hybrid method is used together with the stretched-vortex model (Pullin 2000; Kosović, Pullin & Samtaney 2002) for explicitly modelling the subgrid interaction terms. This approach was also used by Lombardini *et al.* (2011) to study systematically the impact of the Atwood number for a canonical three-dimensional numerical set-up, and for LES of single-shock (i.e. without re-shock) RMI (Lombardini, Pullin & Meiron 2012).

Thornber *et al.* (2010) studied the influence of different three-dimensional broad- and narrow-band multimode initial conditions on the growth rate of a turbulent multicomponent mixing zone developing from RMI. In a later study (Thornber *et al.* 2011), the same authors presented a numerical study of a re-shocked turbulent mixing zone, and extended the theory of Mikaelian and Youngs to predict the behaviour of a multicomponent mixing zone before and after re-shock (cf. Mikaelian 1989; Thornber *et al.* 2010). They used an implicit LES (Drikakis 2003; Thornber *et al.* 2008; Drikakis *et al.* 2009) approach based on a finite-volume Godunov-type method to solve the Euler equations with the same specific heat ratio for both fluids.

In a recent investigation, Weber, Cook & Bonazza (2013) derived a growth-rate model for the single-shock RMI based on the net mass flux through the centre plane of the mixing zone. Here, the compressible Navier–Stokes equations were solved by a tenth-order compact difference scheme for spatial differentiation. Artificial grid-dependent fluid properties, proposed by Cook (2007), were used for shock and material-interface capturing as well as for subgrid-scale modelling.

Grid-resolution-independent statistical quantities of the single-shock RMI were presented by Tritschler *et al.* (2013*a*). The kinetic energy spectra exhibit a Kolmogorov

inertial range with $k^{-5/3}$ scaling. The spatial flux discretisation was performed in characteristic space by an adaptive central-upwind sixth-order-accurate WENO scheme (Hu, Wang & Adams 2010) in the low-dissipation version of Hu & Adams (2011).

LES relies on scale separation, where the energy-containing large scales are resolved and the effect of non-resolved scales is modelled either explicitly or implicitly. However, turbulent mixing initiated by RMI for typical LES mainly occurs at the marginally resolved or non-resolved scales. The interaction of non-resolved small scales with the resolved scales as well as the effect of the interaction of non-resolved scales with themselves is modelled by the employed subgrid-scale model. Moreover, discontinuities such as shock waves and material interfaces need to be captured by the numerical scheme. Owing to the broad range of scales, coarse-grained numerical simulations of RMI strongly rely on the resolution capabilities for the different types of subgrid scales (turbulent small scales, shocks, interfaces) of the underlying numerical scheme.

So far, research has mainly focused on the identification and quantification of parameters that affect the evolution of Richtmyer–Meshkov unstable flows. The influence of the Atwood number (Lombardini *et al.* 2011), the Mach number (Lombardini *et al.* 2012) as well as the specific initial interface perturbations (Schilling & Latini 2010; Thornber *et al.* 2010; Grinstein, Gowardhan & Wachtor 2011) on the temporal evolution of the instability have been investigated. Results from numerical simulations have been compared to experiments (Hill *et al.* 2006; Schilling & Latini 2010; Tritschler *et al.* 2013*b*) and theoretical models have been derived (Thornber *et al.* 2011; Weber *et al.* 2013). These investigations have assumed, based on standard arguments such as empirical resolution criteria, that the marginally and non-resolved scales have a negligible effect on the resolved scales, and therefore on the evolution of the instability. Uncertainties introduced by the numerical method, i.e. the subgrid-scale regularisation and truncation errors, have not yet been investigated systematically. There is, however, strong evidence that numerical model uncertainty can significantly affect the linear and nonlinear stages of evolution, and in particular the mixing measures. In fact, it is unclear how subgrid-scale regularisation and dispersive or dissipative truncation errors can affect the resolved scales and turbulent mixing measures.

In the present investigation, two independently developed and essentially different numerical methods are employed to study the prediction uncertainties of RMI simulations. The first method has a dominantly dissipative truncation error at the non-resolved scales, whereas the second one exhibits a more dispersive behaviour. At the marginally resolved scales, the numerical truncation error is not small and the particular character of the truncation error is essential for the implicit modelling capabilities of the method, and thus also affects the resolved scale solution. For the purpose of investigating this effect, integral and spectral mixing metrics as well as probability density functions are analysed on four computational grids with resolutions ranging from 1562 to 195 µm. The simulations employing two different numerical methods on a very fine grid resolution of 195 µm provide a data set with high confidence in the results.

We emphasise that the purpose of this study is (i) to present RMI results with a clear identification of the resolved scale range by systematic grid refinement, and (ii) to assess the physical effects of numerical subgrid-scale regularisations on the marginally resolved and on the non-resolved scale range. We do not intend to propose or improve a certain subgrid-scale model or regularisation scheme.

The paper is structured as follows. The governing equations along with the employed numerical models are described in §2. Details about the computational

domain and the exact generic initial conditions are given in §3. Results are presented in §4, and the key findings of the present study are discussed in §5.

2. Numerical model

2.1. *Governing equations*

We solve the three-dimensional multicomponent Navier–Stokes equations:

$$\frac{\partial \rho}{\partial t} + \nabla \cdot (\rho \boldsymbol{u}) = 0, \tag{2.1a}$$

$$\frac{\partial (\rho \boldsymbol{u})}{\partial t} + \nabla \cdot (\rho \boldsymbol{u}\boldsymbol{u} + p\boldsymbol{\delta} - \boldsymbol{\tau}) = 0, \tag{2.1b}$$

$$\frac{\partial E}{\partial t} + \nabla \cdot [(E + p)\boldsymbol{u}] - \nabla \cdot (\boldsymbol{\tau} \cdot \boldsymbol{u} - \boldsymbol{q}_c - \boldsymbol{q}_d) = 0, \tag{2.1c}$$

$$\frac{\partial \rho Y_i}{\partial t} + \nabla \cdot (\rho \boldsymbol{u} Y_i) + \nabla \cdot \boldsymbol{J}_i = 0. \tag{2.1d}$$

In (2.1a), $\boldsymbol{u}$ is the velocity vector, p is the pressure, E is the total energy, ρ is the mixture density, Y_i is the mass fraction and $\boldsymbol{J}_i$ is the diffusive mass flux of species $i = 1, 2, \ldots, K$, with K the total number of species. The identity matrix is $\boldsymbol{\delta}$.

The viscous stress tensor $\boldsymbol{\tau}$ for a Newtonian fluid is

$$\boldsymbol{\tau} = 2\bar{\mu}\boldsymbol{S} + (\beta - \tfrac{2}{3}\bar{\mu})\boldsymbol{\delta}(\nabla \cdot \boldsymbol{u}), \tag{2.2}$$

with the mixture viscosity $\bar{\mu}$ and the strain-rate tensor $\boldsymbol{S}$. According to Fourier's law, we define the heat flux as

$$\boldsymbol{q}_c = -\bar{\kappa}\nabla T \tag{2.3}$$

and the inter-species diffusional heat flux (Cook 2009) as

$$\boldsymbol{q}_d = \sum_{i=1}^{K} h_i \boldsymbol{J}_i, \tag{2.4}$$

with

$$\boldsymbol{J}_i \approx -\rho \left(D_i \nabla Y_i - Y_i \sum_{j=1}^{K} D_j \nabla Y_j \right). \tag{2.5}$$

Here D_i indicates the effective binary diffusion coefficient of species i, and h_i is the individual species enthalpy. The equations are closed with the equation of state for an ideal gas,

$$p(\rho e, Y_1, Y_2, \ldots, Y_K) = (\bar{\gamma} - 1)\rho e, \tag{2.6}$$

where $\bar{\gamma}$ is the ratio of specific heats of the mixture and e is the internal energy,

$$\rho e = E - \tfrac{1}{2}\rho \boldsymbol{u}^2. \tag{2.7}$$

The multicomponent as well as the molecular mixing rules for $\bar{\gamma}$, $\bar{\mu}$, D_i and $\bar{\kappa}$ are given in appendices A and B.

2.2. *Numerical methods*

2.2.1. *The Miranda simulation code*

The Miranda simulation code has been used extensively for simulating turbulent flows with high Reynolds numbers and multi-species mixing (Cook, Cabot & Miller 2004; Cabot & Cook 2006; Olson & Cook 2007; Olson *et al.* 2011; Weber *et al.* 2013). Miranda employs a tenth-order compact difference scheme (Lele 1992) for

spatial differentiation and a five-stage fourth-order Runge–Kutta scheme (Kennedy, Carpenter & Lewis 2000) for temporal integration of the compressible multicomponent Navier–Stokes equations. Full details of the numerical method are given by Cook (2007), which includes an eighth-order compact filter that is applied to the conserved variables at each time step and smoothly removes the top 10 % of wavenumbers to ensure numerical stability. For numerical regularisation of non-resolved steep flow gradients, artificial fluid properties are used to damp locally structures that exist on the length scales of the computational mesh. In this approach, artificial diffusion terms are added to the physical ones that appear in equations (2.2), (2.3) and (2.5) as

$$\mu = \mu_f + \mu^*, \tag{2.8}$$
$$\beta = \beta_f + \beta^*, \tag{2.9}$$
$$\kappa = \kappa_f + \kappa^*, \tag{2.10}$$
$$D_i = D_{f,i} + D_i^*. \tag{2.11}$$

This LES method employing artificial fluid properties was originally proposed by Cook (2007), but has been altered by replacing the S (magnitude of the strain rate tensor), with $\nabla \cdot \boldsymbol{u}$ in the equation for β^*. Mani, Larsson & Moin (2009) showed that this modification substantially decreases the dissipation error of the method. Here we give the explicit formulation of the artificial terms on a Cartesian grid,

$$\mu^* = C_\mu \overline{\rho |\nabla^r S|} \Delta^{(r+2)}, \tag{2.12}$$
$$\beta^* = C_\beta \overline{\rho |\nabla^r (\nabla \cdot \boldsymbol{u})|} \Delta^{(r+2)}, \tag{2.13}$$
$$\kappa^* = C_\kappa \overline{\frac{\rho c_s}{T} |\nabla^r e|} \Delta^{(r+1)}, \tag{2.14}$$
$$D_i^* = C_D \overline{|\nabla^r Y_i|} \frac{\Delta^{(r+2)}}{\Delta t} + C_Y \overline{(|Y_i| + |1 - Y_i| - 1)} \frac{\Delta^2}{2\Delta t}, \tag{2.15}$$

where $S = (\boldsymbol{S} : \boldsymbol{S})^{1/2}$ is the magnitude of the strain-rate tensor, $\Delta = (\Delta x \Delta y \Delta z)^{1/3}$ is the local grid spacing, c_s is the sound speed and Δt is the time step size. The polyharmonic operator, ∇^r, denotes a series of Laplacians, e.g. $r = 4$ corresponds to the biharmonic operator, $\nabla^4 = \nabla^2 \nabla^2$. The overbar ($\bar{f}$) denotes a truncated-Gaussian filter applied along each grid direction as in Cook (2007) to smooth out sharp cusps introduced by the absolute value operator. In LES of RMI, β^* acts as the shock-capturing scheme. The μ^* is primarily used as a numerical stabilisation mechanism rather than as a subgrid-scale model. The artificial shear viscosity is found not to be needed to maintain numerical stability in the current calculations and its inclusion has a small impact on the solution. The dissipation of the vortical motion primarily depends on the eighth-order compact filter.

2.2.2. *The INCA simulation code*

The INCA simulation code is a multi-physics simulation method for single- and multicomponent turbulent flows. With respect to the objective in this paper, it has been tested and validated for shock-induced turbulent multi-species mixing problems at finite Reynolds numbers (Tritschler *et al.* 2013*a*,*b*, 2014).

For all the simulations presented in this paper, we use a discretisation scheme that employs for the hyperbolic part in (2.1*a*) a flux projection on local characteristics. The Roe-averaged matrix required for the projection is calculated for the full multi-species

system (Roe 1981; Larouturou & Fezoui 1989; Fedkiw, Merriman & Osher 1997). The numerical fluxes at the cell faces are reconstructed from cell averages by the adaptive central-upwind sixth-order weighted essentially non-oscillatory (WENO-CU6) scheme (Hu *et al.* 2010) in its scale separation formulation by Hu & Adams (2011).

The fundamental idea of the WENO-CU6 scheme is to use a non-dissipative sixth-order central stencil in smooth flow regions and a nonlinear convex combination of third-order stencils in regions with steep gradients. The reconstructed numerical flux at the cell boundaries is computed from

$$\hat{f}_{i+1/2} = \sum_{k=0}^{3} \omega_k \hat{f}_{k,i+1/2}, \qquad (2.16)$$

where ω_k is the weight assigned to stencil k with the second-degree reconstruction polynomial approximation for $\hat{f}_{k,i+1/2}$. In the WENO-CU6 framework the weights ω_k are given by

$$\omega_k = \frac{\alpha_k}{\sum_{k=0}^{3} \alpha_k}, \quad \alpha_k = d_k \left(C + \frac{\tau_6}{\beta_k + \epsilon} \right)^q, \qquad (2.17)$$

with ϵ being a small positive number $\epsilon = 10^{-40}$. The optimal weights d_k are defined such that the method recovers the sixth-order central scheme in smooth flow regions. The constant parameters in (2.17) are set to $C = 1000$ and $q = 4$ (see Hu & Adams 2011), τ_6 is a reference smoothness indicator that is calculated from a linear combination of the other smoothness measures β_k with

$$\tau_6 = \beta_6 - \tfrac{1}{6}(\beta_0 + \beta_2 + 4\beta_1) \qquad (2.18)$$

and

$$\beta_k = \sum_{j=1}^{2} \Delta x^{2j-1} \int_{x-1/2}^{x_{i+1/2}} \left(\frac{\mathrm{d}^j}{\mathrm{d}x^j} \hat{f}_k(x) \right)^2 \mathrm{d}x, \qquad (2.19)$$

and β_6 is also calculated from (2.19) but with the fifth-degree reconstruction polynomial approximation of the flux, which gives the six-point stencil for the sixth-order interpolation.

After reconstruction of the numerical fluxes at the cell boundaries, the fluxes are projected back onto the physical field. A local switch to a Lax–Friedrichs flux is used as entropy fix (see e.g. Toro 1999). A positivity-preserving flux limiter (Hu, Adams & Shu 2013) is employed in regions with low pressure or density, maintaining the overall accuracy of the sixth-order WENO scheme. It has been verified that the flux limiter has negligible effect on the results, and avoids excessively small time step sizes. Temporal integration is performed by a third-order total variation-diminishing Runge–Kutta scheme (Gottlieb & Shu 1998).

3. Numerical set-up

3.1. *Computational domain*

We consider a shock tube with constant square cross-section. The fine-grid domain extends in the y and z directions symmetrically from $-L_{yz}/2$ to $L_{yz}/2$ and in the x direction from $-L_x/4$ to L_x. An inflow boundary condition is imposed far away from
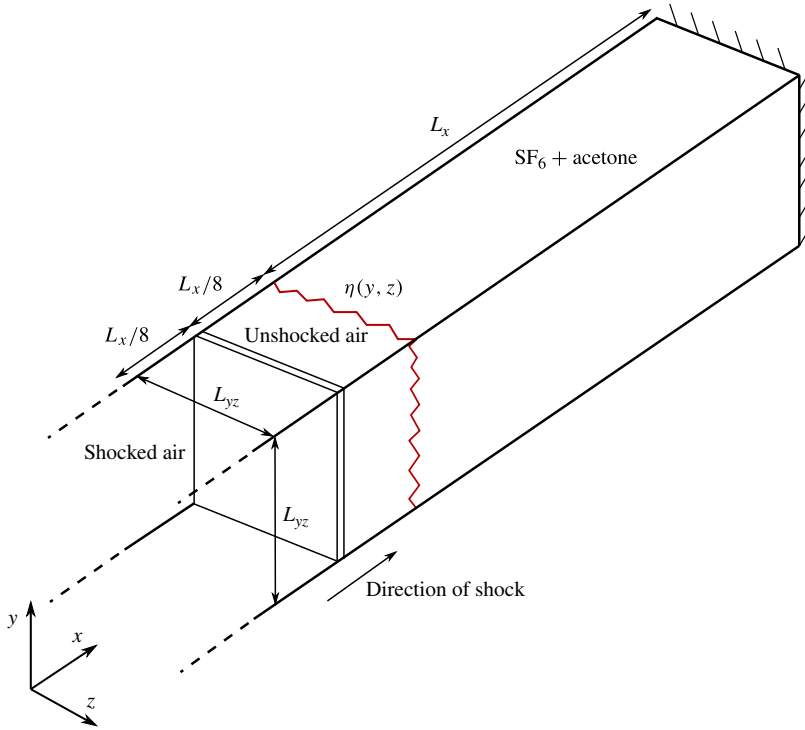
FIGURE 1. (Colour online) Schematic of the square shock tube and dimensions of the computational domain for the simulations.

the fine-grid domain in order to avoid shock reflections. To reduce computational costs, a hyperbolic mesh stretching is applied between the inflow boundary and $-L_x/4$; L_x is set to 0.4 m, and $L_{yz} = L_x/4$. At the boundaries normal to the y and z directions, periodic boundary conditions are imposed and an adiabatic wall boundary at the end of the shock tube at $x = L_x$ is used. A schematic of the computational domain is shown in figure 1.

The fine-grid domain is discretised by four different homogeneous Cartesian grids with 64, 128, 256 and 512 cells in the y and z directions and 320, 640, 1280 and 2560 cells in the x direction, resulting in cubic cells of size 1562 µm $\lesssim \Delta_{xyz} \lesssim$ 195 µm. The total number of cells in the fine-grid domain amounts to $\approx 1.3 \times 10^6$ for the coarsest resolution and to $\approx 670 \times 10^6$ for the finest resolution.

3.2. *Initial conditions*

We consider air as a mixture of nitrogen (N_2) and oxygen (O_2) with (in terms of volume fraction) $X_{N_2} = 0.79$ and $X_{O_2} = 0.21$. The equivalent mass fractions on the air side give $Y_{N_2} = 0.767$ and $Y_{O_2} = 0.233$, i.e. $Y_{air} = Y_{N_2} + Y_{O_2}$. The heavy gas is modelled as a mixture of SF_6 and acetone (Ac) with mass fractions $Y_{SF_6} = 0.8$ and $Y_{Ac} = 0.2$, i.e. $Y_{HG} = Y_{SF_6} + Y_{Ac}$. The material interface between light (air) and heavy gas is accelerated by a shock wave with Mach number $Ma = 1.5$ that is initialised at $x = -L_x/8$ propagating in the positive x direction. The pre-shock state is defined by the stagnation condition $p_0 = 23\,000$ Pa and $T_0 = 298$ K. The corresponding post-shock

Quantity	Post-shock	Pre-shock light-gas side	Pre-shock heavy-gas side
ρ (kg m^{-3})	0.498 69	0.267 84	1.040 57
U (m s^{-1})	240.795	0	0
p (Pa)	56 541.7	23 000	23 000
T (K)	393.424	298	298
D_{N_2} (m^2 s^{-1})	5.919×10^{-5}	8.981×10^{-5}	—
D_{O_2} (m^2 s^{-1})	5.919×10^{-5}	8.981×10^{-5}	—
D_{SF_6} (m^2 s^{-1})	—	—	1.846×10^{-5}
D_{Ac} (m^2 s^{-1})	—	—	1.846×10^{-5}
$\bar{\mu}$ (Pa s)	2.234×10^{-5}	1.826×10^{-5}	1.328×10^{-5}
$\overline{c_p}$ (J kg^{-1} K^{-1})	1008.35	1008.35	815.89

TABLE 1. Initial values of the post-shock state and the pre-shock states of the light- and heavy-gas sides.

thermodynamic state is obtained from the Rankine–Hugoniot conditions,

$$\rho'_{air} = \rho_{air} \frac{(\gamma_{air} + 1)Ma^2}{2 + (\gamma_{air} - 1)Ma^2}, \tag{3.1a}$$

$$u'_{air} = Ma\, c_{air} \left(1 - \frac{\rho_{air}}{\rho'_{air}} \right), \tag{3.1b}$$

$$p'_{air} = p_0 \left(1 + 2\frac{\gamma_{air}}{\gamma_{air} + 1}(Ma^2 - 1) \right), \tag{3.1c}$$

with $c_{air} = \sqrt{\gamma_{air} p_0 / \rho_{air}}$. The initial data of the post-shock state of the light gas as well as the pre-shock state of the light and heavy gases are given in table 1.

Tritschler *et al.* (2013*a*) introduced a generic initial perturbation of the material interface that resembles a stochastic random perturbation but being, however, deterministic and thus exactly reproducible for different simulation runs. This multimode perturbation is given by the function

$$\eta(y, z) = a_1 \sin(k_0 y) \sin(k_0 z) + a_2 \sum_{n=1}^{13} \sum_{m=3}^{15} a_{n,m} \sin(k_n y + \phi_n) \sin(k_m z + \chi_m) \tag{3.2}$$

with the constant amplitudes $a_1 = -0.0025$ m and $a_2 = 0.000\,25$ m and wavenumbers $k_0 = 10\pi/L_{yz}$, $k_n = 2\pi n/L_{yz}$ and $k_m = 2\pi m/L_{yz}$. The amplitudes $a_{n,m}$ and the phase shifts ϕ_n and χ_m are given by

$$a_{n,m} = \sin(nm)/2, \tag{3.3a}$$

$$\phi_n = \tan(n), \tag{3.3b}$$

$$\chi_m = \tan(m). \tag{3.3c}$$

To facilitate a grid sensitivity study, we impose an initial length scale by prescribing a finite initial interface thickness in the mass fraction field as

$$\psi(x, y, z) = \frac{1}{2} \left(1 + \tanh\left(\frac{x - \eta(y, z)}{L_\rho} \right) \right) \tag{3.4}$$
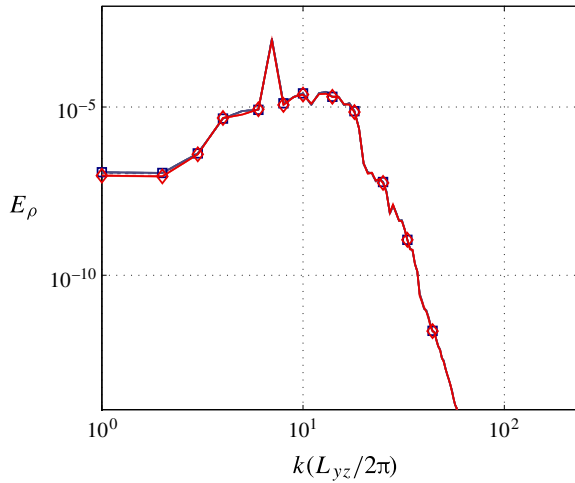
FIGURE 2. (Colour online) Initial power spectra of density from Miranda (dark grey; blue online) and INCA (light grey; red online). The different resolutions are represented as dotted line (64), dashed line (128), solid line (256) and solid line with open squares for Miranda and open diamonds for INCA (512).

with $L_\rho = 0.01$ m being the characteristic initial thickness. The individual species mass fractions are set as

$$Y_{SF_6} = 0.8\psi, \quad Y_{Ac} = 0.2\psi, \quad (3.5a,b)$$

$$Y_{N_2} = 0.767(1 - \psi), \quad Y_{O_2} = 0.233(1 - \psi). \quad (3.6a,b)$$

The material interface is initialised at $x - \eta(y, z) = 0$ m. Combined with the multicomponent and molecular mixing rules given in appendices A and B, the flow field is fully defined at $t = 0$.

Figure 2 shows the initial condition in terms of the power spectrum of density for Miranda and INCA at all grid resolutions. The initial perturbation given in (3.2) and shown in figure 2 has been designed with the objective to obtain a reproducible and representative data set. Nevertheless, we cannot exclude the possibility that some of the observations presented in this paper do not apply to very different initial perturbations.

4. Results

To explore the effect of the finite truncation error arising from grid resolution and numerical method, four meshes were used to compute the temporal evolution of RMI with both Miranda and INCA. The simulation reaches $t = 6.0$ ms, which is well beyond the occurrence of re-shock at $t \approx 2$ ms. At this stage, the effects of reflected shock waves and expansion waves on the shock location have become small, as the shock wave is attenuated with each subsequent reflection. The space–time $(x$–$t)$ diagram shown in figure 3 depicts the propagation of the shock wave and interface during the simulation.

The initial conditions described in the previous section are entirely deterministic and, owing to their band-limited representations, are identically imposed at the different grid resolutions and for the two numerical methods. Therefore, the obtained results
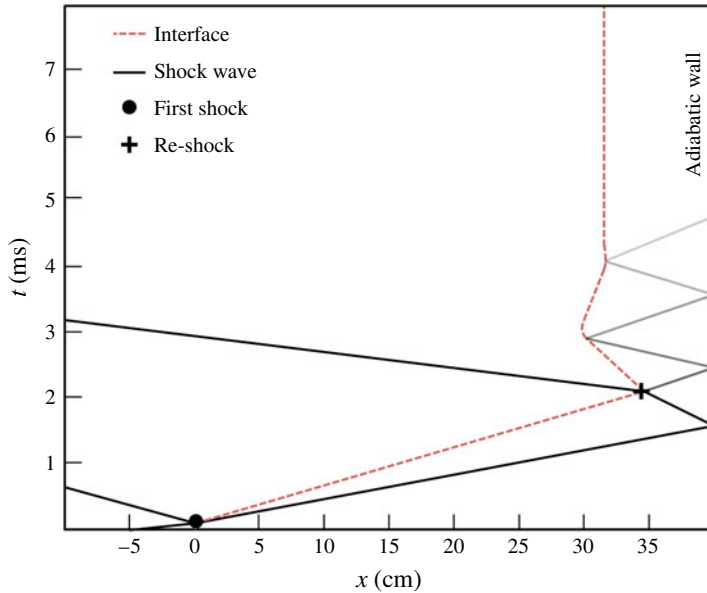
FIGURE 3. (Colour online) Space–time (x–t) diagram depicting the propagation of the shock wave and interface during the simulation. The effect of the shock wave on the interface location is attenuated with each subsequent reflection.

exhibit uncertainties due only to the numerical method and to grid resolution, but exclude initial-data uncertainties.

For illustration we show the three-dimensional contour plots of species mass fraction of the heavy gas Y_{HG} obtained with Miranda and INCA, respectively, in figure 4. Similarities at the large scales are clearly visible after re-shock, but also differences exist at the fine scales, more clearly visible from the inset.

4.1. *Integral quantities*

Integral measures of the mixing zone are presented here for both numerical models and all resolutions. Often, these time-dependent integral measures are the only metrics available for comparison with experiment and are therefore of primary importance for validation.

Figure 5 shows the transition process predicted by the reference grid with a resolution of 512 cells in the transverse directions. The numerical challenge, prior to re-shock, is to predict the large-scale nonlinear entrainment and the associated interface steepening. The interface eventually becomes under-resolved when its thickness reaches the resolution limit of the numerical scheme and further steepening is prevented by numerical diffusion. The equilibrium between interface steepening and numerical diffusion occurs later in time as the grid is refined. The accurate prediction of the interface steepening phenomenon is one of the main challenges in modelling pre-transitional RMI where large-scale flow structures are still regular. This is because the numerical model largely determines the time when mixing transition occurs. In nature, mixing transition is due to the presence of small-scale perturbations, whereas in numerical simulation, the transition is triggered by backscatter from the under-resolved scales as predicted by the particular numerical model. Hence, details of mixing transition of the material interface evolve differently for the two codes.
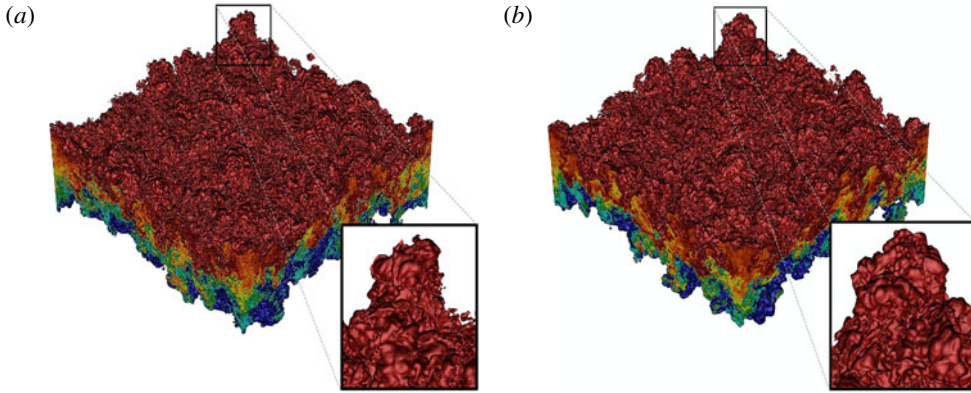
FIGURE 4. (Colour online) Three-dimensional contour plots of species mass fraction of the heavy gas from (*a*) Miranda and (*b*) INCA data. Data are from the finest grid at $t = 2.5$ ms that show contours of the heavy-gas mass fraction Y_{HG} from 0.1 (at the bottom; blue online) to 0.9 (at the top; red online). Note that, although some large-scale features remain consistent between codes, small and intermediate scales are quite different at this stage.
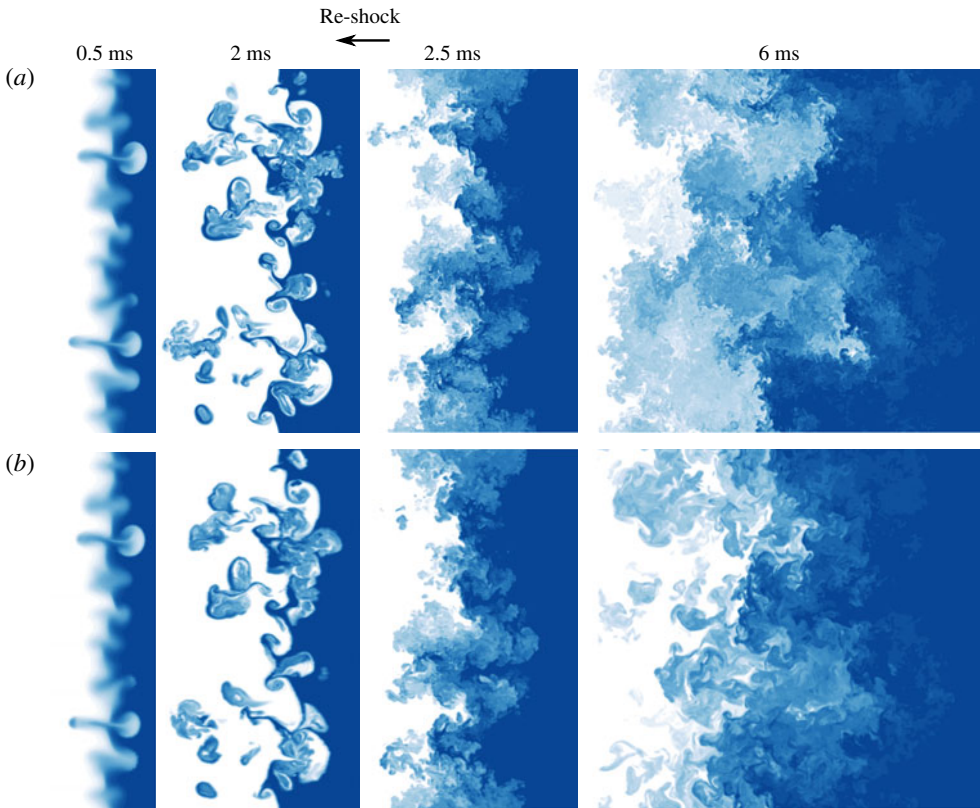

FIGURE 5. (Colour online) Colour-coded plots of species mass fraction of SF_6 gas from (*a*) Miranda and (*b*) INCA at various times where data are taken from the finest grid. The contours range from 0.05 (white) to 0.75 (dark grey; blue online).
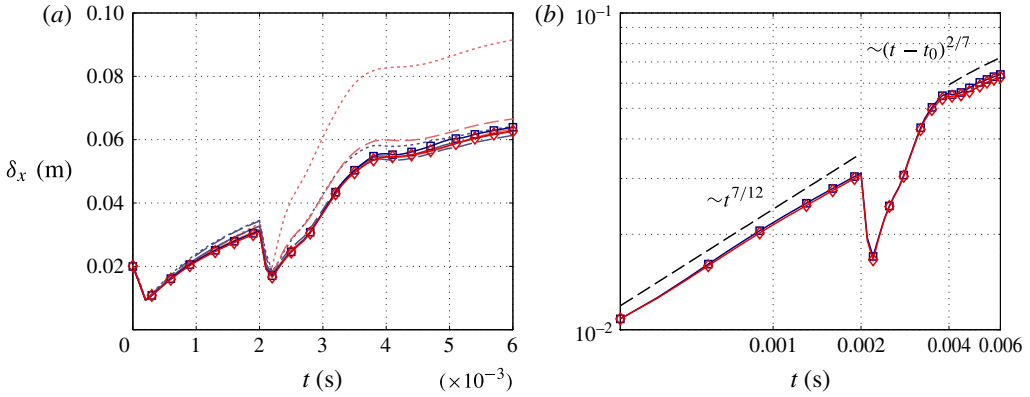
FIGURE 6. (Colour online) Time evolution of the mixing zone width from Miranda (dark grey; blue online) and INCA (light grey; red online). The different resolutions are represented as dotted line (64), dashed line (128), solid line (256) and solid line with open squares for Miranda and open diamonds for INCA (512).

Nevertheless, similarities before re-shock are striking and large-scale similarities in the resolved wavenumber range even persist throughout the entire simulation time. Following re-shock, the large interfacial scales break down into smaller scales and develop a turbulent mixing zone as can be seen in figures 4 and 5. By visual inspection of figure 5, one finds that the post-re-shock turbulent structures are very similar, whereas the long-term evolution of the small scales appears to be different between the codes. Differences in the observed flow field at $t = 6$ ms may indicate slightly different effective Reynolds numbers for the two numerical methods and therefore they also exhibit different decay rates of enstrophy (Dimotakis 2000; Lombardini *et al.* 2012), as can be seen in figure 8 after re-shock.

The mixing width δ_x is a length scale that approximates the large-scale temporal evolution of the turbulent mixing zone. It is defined as an integral measure by

$$\delta_x(t) = \int_{-\infty}^{\infty} 4\phi(1-\phi)\mathrm{d}x, \quad \text{with } \phi(x, t) = \langle Y_{\mathrm{SF}_6} + Y_{\mathrm{Ac}} \rangle_{yz}, \quad (4.1)$$

where $\langle \cdot \rangle_{yz}$ denotes the ensemble average in the cross-stream yz plane. For a quantity φ it is defined by

$$\langle \varphi \rangle_{yz}(x, t) = \frac{1}{\mathscr{A}} \iint \varphi(x, y, z, t) \, \mathrm{d}y \, \mathrm{d}z, \quad \text{with } \mathscr{A} = \iint \mathrm{d}y \, \mathrm{d}z. \quad (4.2)$$

The mixing width plotted in figure 6(*a*) shows that data from both numerical methods converge to a single solution throughout the entire simulation time. Furthermore, it is observed that even with very-high-order models a minimum resolution of ~ 400 µm appears to be necessary for an accurate prediction of the mixing zone width. As will be shown later, coarser grids tend to overpredict not only the growth of the mixing zone but also molecular mixing.

Figure 6(*b*) shows the mixing zone width time evolution on a log–log scale. The (bubble) growth-rate model of Zhou (2001) predicts accurately the pre-re-shock mixing zone growth rate that is consistently recovered by both numerical methods as $\sim t^{7/12}$. However, this is, according to Zhou (2001), the growth rate that is associated with turbulence of Batchelor type (Batchelor & Proudman 1956) with $E(k) \sim k^4$

as $k \to 0$. The kinetic energy spectra in the present investigation are of Saffman type (Saffman 1967*a*,*b*) with $E(k) \sim k^2$ as $k \to 0$ (Tritschler *et al.* 2013*a*), for which Zhou (2001) predicts a growth that scales with $\sim t^{5/8}$. The present growth rates are also in good agreement with the experimental and numerical results of Dimonte, Frerking & Schneider (1995) with $\sim t^\beta$ and $\beta = 0.6 \pm 0.1$ and their model predictions $\sim (t - t_i)^{1/2}$, where t_i accounts for the time the shock needs to traverse the interface. As the mixing zone has not yet reached self-similar evolution, the initial growth rate depends on the specific initial conditions.

Llor (2006) found that the self-similar growth rate of the energy-containing eddies, i.e. the integral length scale, for incompressible RMI at vanishing Atwood number, should scale as $\delta_x \sim t^{1-n/2}$ with $2/7 \leqslant 1 - n/2 \leqslant 1/3$, if the turbulence kinetic energy (TKE) decays as $\sim t^{-n}$. These growth rates slightly differ from the growth-rate prediction for homogeneous isotropic turbulence, $1/3 \leqslant 1 - n/2 \leqslant 2/5$, by the same author. The predictions of Llor (2006), however, are at odds with Kolmogorov's classical decay law (Kolmogorov 1941) for TKE $\sim t^{-10/7}$ and more recent investigations of decaying isotropic turbulence by Ishida, Davidson & Kaneda (2006) and Wilczek, Daitche & Friedrich (2011), which found Kolmogorov's decay law to hold if the Loitsyansky integral is constant and if the Taylor-scale Reynolds number exceeds $Re_\lambda \geqslant 100$. Based on Rayleigh–Taylor experiments driven by either sustained or impulsive acceleration at various Atwood numbers, Dimonte & Schneider (2000) found scaling laws for the bubble and spike growth rate. For the present density ratio, the exponents become $1 - n_B/2 \approx 0.25 \pm 0.05$ for the former and $0.25 \leqslant 1 - n_S/2 \leqslant 0.43$ for the latter. The late-time mixing zone growth rate is therefore expected to correlate with the spike growth rate. The late-time growth-rate prediction of the present work is $\sim (t - t_0)^{2/7}$, i.e. $1 - n/2 = 2/7$, once the turbulent mixing zone is fully established. Time t_0 is a virtual time origin set to $t_0 = 2$ ms. This is consistent with the mixing zone width growth-rate predictions of Llor (2006) and the late-time growth-rate predictions of Dimonte & Schneider (2000), but underestimates the predictions of Zhou (2001), with a scaling of $t^{1-n/2}$ with $0.35 \leqslant 1 - n/2 \leqslant 0.45$ long after re-shock, once the nonlinear time scale has become the dominant time scale. In the numerical investigation of Lombardini *et al.* (2012), the authors found the mixing zone width to grow as $0.2 \leqslant 1 - n/2 \leqslant 0.33$. Before re-shock the infrared part of the kinetic energy spectrum (see figure 14) exhibits a k^2 range, for which a post-re-shock growth rate of $\sim t^{2/7}$ is predicted by the model of Youngs (2004), which is in good agreement with the present data.

The definition of the molecular mixing fraction Θ (Youngs 1991, 1994) is given as

$$\Theta(t) = \frac{\displaystyle\int_{-\infty}^{\infty} \langle X_{air} X_{HG} \rangle_{yz} \, \mathrm{d}x}{\displaystyle\int_{-\infty}^{\infty} \langle X_{air} \rangle_{yz} \langle X_{HG} \rangle_{yz} \, \mathrm{d}x} \tag{4.3}$$

and quantifies the amount of mixed fluid within the mixing zone. It can be interpreted as the ratio of molecular mixing to large-scale entrainment by convective motion.

As bubbles of light air and spikes of heavy gas begin to interfuse, the initially mixed interface between the fluids steepens and the fluids become more segregated on the molecular level (see figure 7*a*). The molecular mixing fraction reaches its minimum at $t \approx 1.3$ ms before Kelvin–Helmholtz instabilities lead to an increase of molecular mixing. The onset of secondary instabilities is very sensitive to the numerical method, as the numerical scheme determines how sharp the material interface can be represented or whether numerical diffusion or dispersion effects lead to an early mixing transition.
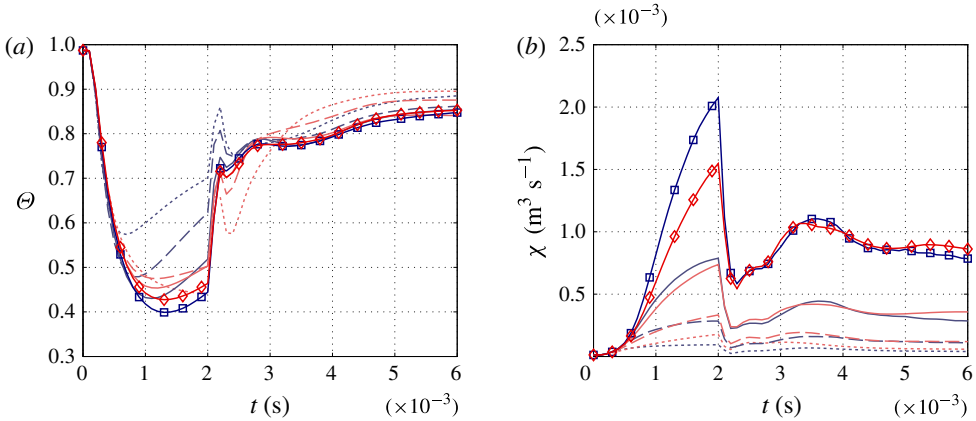
FIGURE 7. (Colour online) Molecular mixing fraction Θ and scalar dissipation rate χ from Miranda (dark grey; blue online) and INCA (light grey; red online). The different resolutions are represented as dotted line (64), dashed line (128), solid line (256) and solid line with open squares for Miranda and open diamonds for INCA (512).

After re-shock molecular mixing is strongly enhanced and reaches its maximum of $\Theta \approx 0.85$ by the end of the simulation. This finding is consistent with Lombardini *et al.* (2012), who also found an asymptotic late-time mixing behaviour with $\Theta \approx 0.85$ independent of the shock Mach number but without re-shock. The asymptotic limit is already accurately calculated on grid resolutions of ~ 400 µm. As the second shock wave compresses the mixing zone, the instability becomes less entrained yet equally diffused (at least in the y and z directions) and therefore causes a steep rise in Θ. A gradual increase of the mixing fraction after the steep rise occurs as the mixing zone becomes more homogeneously distributed (Thornber *et al.* 2011) due to turbulent motion.

The temporal evolution of the scalar dissipation rate is plotted in figure 7(*b*) and is derived from the advection–diffusion equation for a scalar. The instantaneous scalar dissipation rate of the three-dimensional RMI is estimated from the SF_6 concentration field as

$$\chi(t) = \int_{-\infty}^{\infty} D_{SF6} \nabla Y_{SF6} \cdot \nabla Y_{SF6} \, dx \, dy \, dz, \qquad (4.4)$$

which quantifies the rate at which mixing occurs. For consistency of post-processing, a second-order central difference scheme has been used for the calculation of the spatial derivatives in (4.4) and (4.6) for all simulation data sets. Note that the order of the finite difference scheme with which the gradients in (4.4) and (4.6) are approximated affect their results.

The variation of the scalar dissipation rate with grid resolution before re-shock is largely due to the under-resolved material interface and the onset of mixing transition. Mixing is strongly enhanced after the second shock–interface interaction, but the mixing zone is also confined to a much smaller region, which results in a decrease of the integral χ. Also, χ only represents the resolved part of the dissipation rate and therefore certainly underestimates the true value.

The TKE and the enstrophy (ε) are integrated over cross-flow planes in the mixing zone that satisfy

$$4\phi[1 - \phi] \geqslant 0.9. \qquad (4.5)$$

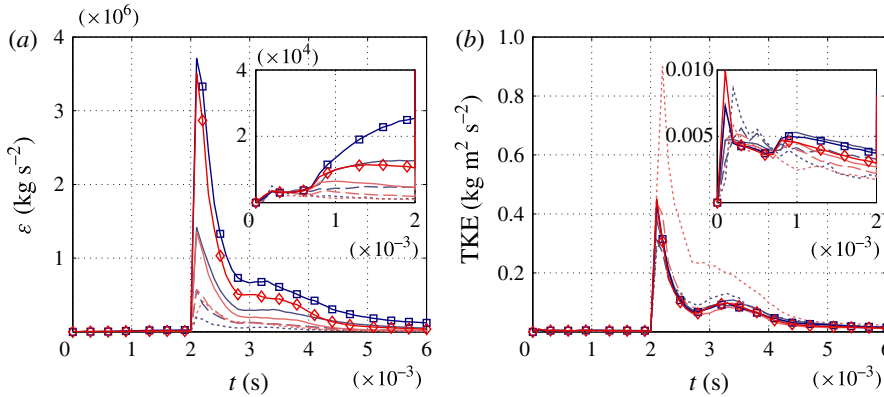This region is referred to as the inner mixing zone (IMZ) in the following.

FIGURE 8. (Colour online) Enstrophy ε and turbulence kinetic energy (TKE) from Miranda (dark grey; blue online) and INCA (light grey; red online). The different resolutions are represented as dotted line (64), dashed line (128), solid line (256) and solid line with open squares for Miranda and open diamonds for INCA (512).

Baroclinic vorticity is deposited at the material interface during shock passage. The amount of generated vorticity scales directly with the pressure gradient of the shock wave and the density gradient of the material interface. The enstrophy is calculated by

$$\varepsilon(t) = \int_{IMZ} \rho(\omega_i \omega_i) \, dx \, dy \, dz, \qquad (4.6)$$

where ω_i is the vorticity.

As can be seen from figure 8, the enstrophy also exhibits a strong grid dependence. Fully grid-converged results are only obtained for times up to $t \approx 0.7$ ms. As the interface steepens due to strain and shear, the effective interface thickness is determined by numerical diffusion, which appears to occur at $t \approx 0.7$ ms. This is consistent with the evolution of Θ shown in figure 7(a). Following Youngs (2007) and Hahn *et al.* (2011), integration of enstrophy with a theoretical scaling of $k^{1/3}$ up to the cut-off wavenumber yields a proportionality between enstrophy and grid resolution as $\varepsilon \propto \Delta_{xyz}^{-4/3}$. From this follows an increase of enstrophy by a factor of approximately 2.5 from one grid resolution to the next finer, which is in good agreement with the present data.

The amount of TKE created by the impulsive acceleration of the interface is calculated as

$$\text{TKE}(t) = \int_{IMZ} K \, dx \, dy \, dz, \quad \text{with } K(x, y, z, t) = \frac{\rho}{2} u_i'' u_i''. \qquad (4.7)$$

The fluctuating part φ'' of a quantity φ is calculated from

$$\varphi'' = \varphi - \bar{\varphi}, \quad \text{with } \bar{\varphi} = \langle \rho\varphi \rangle_{yz} / \langle \rho \rangle_{yz}, \qquad (4.8)$$

where $\bar{\varphi}$ is the Favre average of φ.

Grid-converged TKE is obtained on grids with a minimum resolution of ~ 400 μm (see figure 8). This is consistent with the convergence rate of the mixing zone width. The total TKE deposited in the IMZ by the first shock–interface interaction can be seen in the inset of figure 8. The re-shock occurring at $t \approx 2$ ms deposits approximately 40 times more TKE than the initial shock wave. Hill *et al.* (2006)
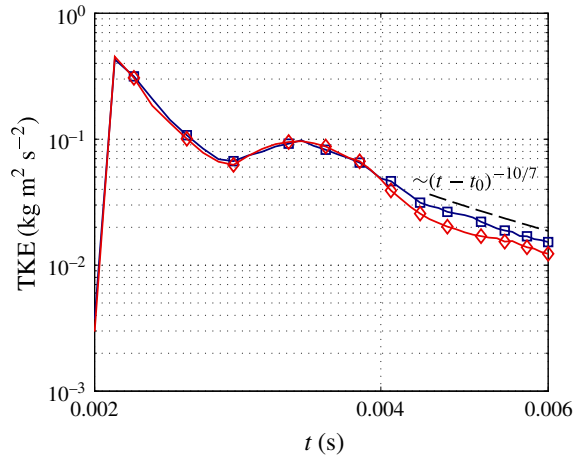
FIGURE 9. (Colour online) Log–log representation of TKE from Miranda (squares; blue online) and INCA (diamonds; red online) taken from the finest grid (512).

found a similar relative increase by the re-shock at the same shock Mach number. A significant decay in energy occurs immediately following re-shock. The material interface interacts with the first expansion fan (see figure 3) and results in a further increase in TKE between 3 and 3.5 ms. The amount of energy deposited by the first expansion wave, however, is much weaker than that deposited by the reflected shock wave. Hill *et al.* (2006) and Grinstein *et al.* (2011) found the amplification of TKE by the first rarefaction to be much stronger than for our data. Such differences are not surprising, because Grinstein *et al.* (2011) reported a strong dependence of energy deposition on the respective initial interface perturbations. After the first expansion wave has interacted with the interface, TKE decays slowly and the pressure gradients associated with the subsequent rarefactions are too shallow to generate any further noticeable increase in TKE.

Lombardini *et al.* (2012) found the decay rate of TKE to be larger than $\sim t^{-6/5}$, approaching $\sim t^{-10/7}$. In our data, the late-time TKE decay is also approximately $\sim (t - t_0)^{-10/7}$, with $t_0 = 2$ ms being the virtual time origin (see figure 9). This scaling would be characteristic for Batchelor-type turbulence (Batchelor & Proudman 1956) with a constant Loitsyansky integral (Kolmogorov 1941; Ishida *et al.* 2006) in contrast to $\sim t^{-6/5}$ typical for turbulence of Saffman type (Saffman 1967*a*,*b*).

In the limit of a self-similar quasi-isotropic state, the temporal evolution of the integral length scale δ_x is related to the evolution of TKE in the mixing zone. From TKE $\propto t^{-n}$, the growth rate of the integral scale follows as $\delta_x \propto t^{1-n/2}$. Llor (2006) derived a maximum decay rate of TKE $\sim t^{-10/7}$ that corresponds to a growth-rate scaling of the energy-containing eddies of $\delta_x \sim t^{2/7}$. These predictions are in excellent agreement with the growth-rate predictions of the mixing zone width of the present investigation (see figure 6) and the decay rate of TKE (see figure 9).

The scalings indicated for the growth rate of the mixing zone and the decay rate of TKE in figures 6 and 9 were not fitted in a strict sense. They merely serve as reference for comparison with incompressible isotropic decaying turbulence. The narrow data range of only ≈ 2 ms after re-shock for which the flow exhibits a self-similar regime precludes any precise estimates for decay and growth-rate laws.
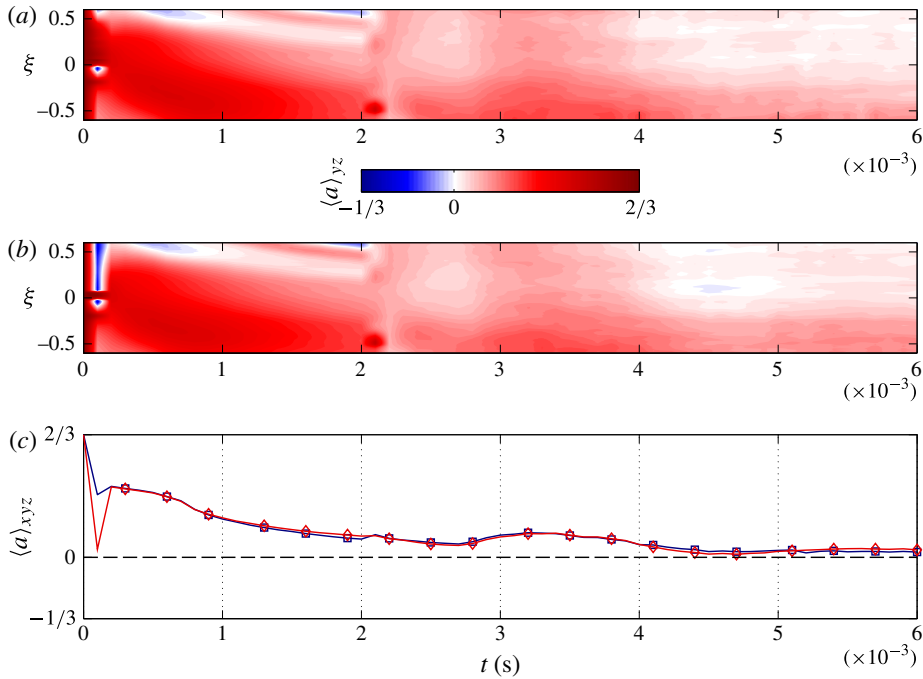
FIGURE 10. Anisotropy $\langle a \rangle_{yz}$ as a function of the dimensionless mixing zone coordinate ξ and time from (a) Miranda and (b) INCA. (c) The volume-averaged anisotropy $\langle a \rangle_{xyz}$ of the inner mixing zone from Miranda (squares) and INCA (diamonds). All data are taken from the finest grid (512).

4.2. *Anisotropy and inhomogeneity of the mixing zone*

In the following, the anisotropy in the mixing zone is investigated. We define the local anisotropy as

$$a(x, y, z, t) = \frac{|u''|}{|u''| + |v''| + |w''|} - \frac{1}{3}, \qquad (4.9)$$

where $a = 2/3$ corresponds to having all TKE in the streamwise velocity component u'', whereas $a = -1/3$ corresponds to having no energy in the streamwise u'' component. In figure 10(a,b) we show the yz plane averaged anisotropy $\langle a \rangle_{yz}$ as a function of the dimensionless mixing zone coordinate ξ and time from Miranda and INCA. The dimensionless mixing zone coordinate ξ is defined as

$$\xi = \frac{x - x^*(t)}{\delta_x(t)}, \qquad (4.10)$$

with $x^*(t)$ being the x location where $4(1 - \phi(x, t))\phi(x, t)$ is maximal.

The light-gas side of the mixing zone remains more anisotropic than the heavy-gas side but with a homogeneous anisotropy distribution after re-shock on either side. The volume-averaged anisotropy in the inner mixing zone $\langle a \rangle_{xyz}$ is shown in figure 10(c). No full recovery of isotropy of the mixing zone is achieved, and the re-shock does not significantly contribute in the sense of the volume-averaged quantity $\langle a \rangle_{xyz}$, but leads to a stratified anisotropy distribution around the centre of the mixing zone. After $t \approx 4.5$ ms an asymptotic limit of $\langle a \rangle_{xyz} \approx 0.04$ is reached, which

temporally coincides with the onset of the self-similar decay of TKE (see figures 9 and 10). The positive value of $\langle a \rangle_{xyz}$ implies that the streamwise component u'' remains, despite re-shock, the dominant velocity component throughout the simulation time. Lombardini *et al.* (2012) also found a temporal asymptotic limit of the isotropisation process in their simulations. Grinstein *et al.* (2011) observed that the velocity fluctuations in the mixing zone are more isotropic when the initial interface perturbations also include short wavelengths, in which case the authors nearly recovered full isotropy. When Grinstein *et al.* (2011) used long-wavelength perturbations, the mixing zone remained anisotropic except for a narrow range on the heavy-gas side.

In order to quantify the homogeneity of mixing, we calculate the density-specific volume correlation (Besnard *et al.* 1992)

$$\langle b \rangle_{yz}(\xi, t) = \left\langle -\left(\frac{1}{\rho}\right)'' \rho'' \right\rangle_{yz} = \left\langle \frac{1}{\rho} \right\rangle_{yz} \langle \rho \rangle_{yz} - 1, \qquad (4.11)$$

which is non-negative. The value $\langle b \rangle_{yz} = 0$ corresponds to homogeneously mixed fluids with constant pressure and temperature. Large values indicate spatial inhomogeneities in the respective yz plane. The density-specific volume correlation has gained some attention in recent years and was the subject of several experimental investigations of the RMI – see Balakumar *et al.* (2012), Balasubramanian *et al.* (2012), Balasubramanian, Orlicz & Prestridge (2013), Orlicz, Balasubramanian & Prestridge (2013), Tomkins *et al.* (2013) and Weber *et al.* (2014).

Figure 11(*a,b*) shows the density-specific volume correlation normalised by the maximal value at time t,

$$\widetilde{\langle b \rangle}_{yz} = \langle b \rangle_{yz}(\xi, t)/\max(\langle b \rangle_{yz})(t), \qquad (4.12)$$

as a function of the dimensionless mixing zone coordinate ξ and time from Miranda and INCA. The largest values of $\widetilde{\langle b \rangle}_{yz}$ are found around the centre of the mixing zone slightly shifted towards the heavy-gas side. The value of $\widetilde{\langle b \rangle}_{yz}$ peaks around the region where mixing between light and heavy gas occurs and tends to zero outside the mixing region, towards the respective pure-gas side. Weber *et al.* (2014) observed in their experiment that the peak of the density-specific volume correlation is initially shifted towards the light-gas side, but moves towards the centre of the mixing zone with increasing time.

In contrast to the anisotropy, where the re-shock does not contribute to the isotropisation and which levels out after $t \approx 4.5$ ms, the mixing zone becomes significantly more homogeneous after re-shock, as can be observed from the temporal evolution of the volume average of the density-specific volume correlation in the inner mixing zone $\langle b \rangle_{xyz}$. Following re-shock the fluids become more and more mixed (see figure 11*c*), with a value of $\langle b \rangle_{xyz} \approx 0.13$ at the latest time. The measured values of the density-specific volume correlation in the single shock–interface interaction experiment of Weber *et al.* (2014) at $Ma = 2.2$ are in good agreement with our simulated values at late times $O(0.1)$, whereas at the lower Mach number $Ma = 1.6$ Weber *et al.* (2014) observed a more inhomogeneous mixing zone $O(0.2)$. These values are significantly larger than those measured for instance in the shock-gas-curtain experiments of Orlicz *et al.* (2013) and Tomkins *et al.* (2013).

4.3. *Spectral quantities*

From homogeneous isotropic turbulence, it is well known that vorticity exhibits coherent worm-like structures with diameter of the order of the Kolmogorov length
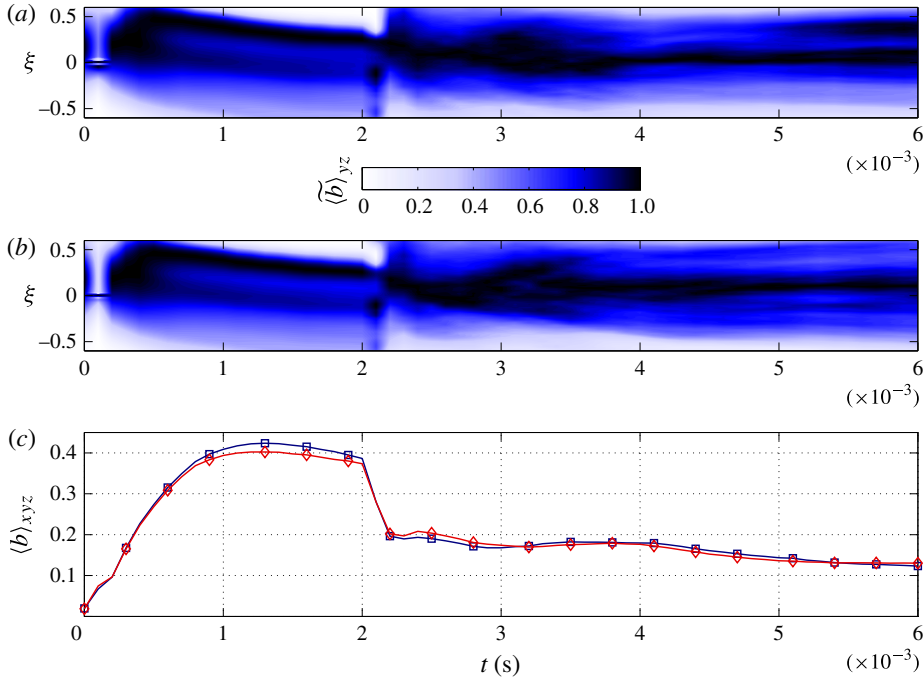
FIGURE 11. (Colour online) Normalised density-specific volume correlation $\widetilde{\langle b \rangle}_{yz}$ as a function of the dimensionless mixing zone coordinate ξ and time from (*a*) Miranda and (*b*) INCA. (*c*) The volume-averaged density-specific volume correlation $\langle b \rangle_{xyz}$ of the inner mixing zone from Miranda (squares) and INCA (diamonds). All data are taken from the finest grid (512).

scale and of a length that scales with the integral scale of the flow. The work of Jiménez *et al.* (1993) suggests that these structures are especially intense features of the background vorticity and independent of any particular forcing that generates the vorticity. In contrast to forced homogeneous isotropic turbulence, where self-similar stationary statistics are achieved, shock-induced turbulent mixing is an inhomogeneous anisotropic unsteady decay phenomenon. Nevertheless, homogeneous isotropic turbulence is used as theoretical framework for most of the numerical analysis of RMI. However, it is unclear at what time and at what locations the mixing zone exhibits the appropriate features and if homogeneous isotropic turbulence is achieved at all. A fully isotropic mixing zone is never obtained, as the anisotropy, even though decreasing with time, reaches an asymptotic limit at $t \approx 4.5$ ms.

The temporal evolution of the initial perturbation is depicted in figure 12. Before re-shock the dominant modes of the initial perturbation slowly break down. After re-shock, however, the additional vorticity deposited during the second shock–interface interaction rapidly destroys structures generated by the initial perturbation and initial shock, leading to a self-similar decay after $t \approx 4$ ms.

Thornber *et al.* (2010, 2012) found, formally in the limit of infinite Reynolds numbers, a persistent $k^{-3/2}$ scaling of the TKE spectrum as well as a $k^{-3/2}$ spectrum with a $k^{-5/3}$ spectrum at high wavenumbers that covers more and more of the spectrum as time proceeds. Furthermore, the same authors (Thornber *et al.* 2011) found (depending on the initial conditions) a $k^{-5/3}$ or a k^{-2} scaling range after
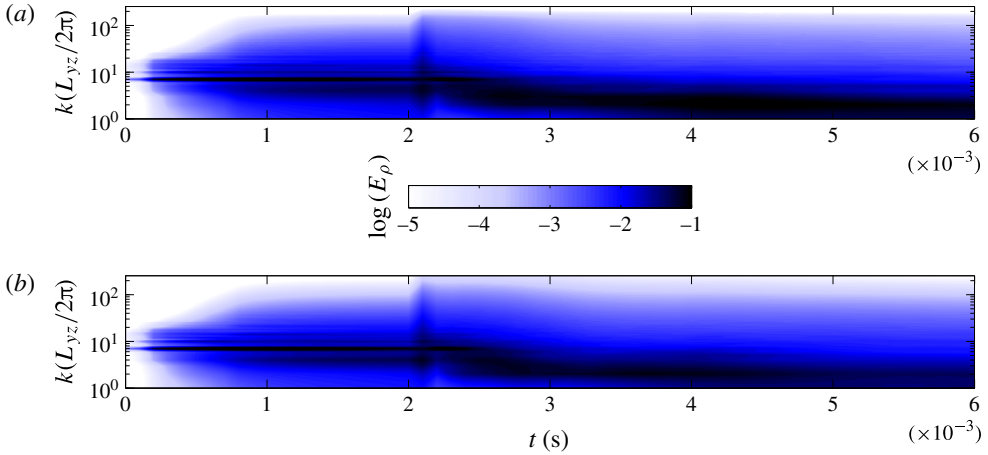
FIGURE 12. (Colour online) Power spectra of density from (*a*) Miranda and (*b*) INCA as a function of wavenumber $k(L_{yz}/2\pi)$ and time. The data are taken from the finest grid (512).

re-shock. Long after re-shock, however, these scalings return to a $k^{-3/2}$ scaling at intermediate scales and to a $k^{-5/3}$ scaling at high wavenumbers, close to the cut-off wavenumber. The authors evaluated the radial spectra either in the centre of the mixing zone or averaged over a fixed number of yz planes within the mixing zone. A different scaling behaviour was observed by Hill *et al.* (2006) and Lombardini *et al.* (2012), who found in their multicomponent LES at finite Reynolds numbers a $k^{-5/3}$ scaling in the centre of the mixing zone, whereas Cohen *et al.* (2002) found a $k^{-6/5}$ scaling range for the single-shock RMI averaged over four transverse slices within the mixing zone. In a recent experimental investigation of a shock-accelerated shear layer, Weber *et al.* (2012) showed a $k^{-5/3}$ inertial range followed by an exponential decay in the dissipation range of the scalar spectrum. This result was numerically reproduced by Tritschler *et al.* (2013*a*). Here, the authors averaged over a predefined IMZ.

All spectra shown in this section are radial spectra with a radial wavenumber that is defined as $k = (k_y^2 + k_z^2)^{1/2}$. The radial spectra are averaged over all yz planes within the IMZ in the x direction that satisfy the condition in (4.5).

The radial power spectra of density are plotted in figure 13, where 13(*a,b*) show the spectra before and 13(*c,d*) after re-shock. The power spectra of density and mass fraction concentration (not shown) show a close correlation, even though they are not directly related, as the mass fractions are constrained to be between zero and one.

Before re-shock, the dominant initial modes slowly break down and redistribute energy to smaller scales. Re-shock causes additional baroclinic vorticity production with inverse sign that results in a destruction process of the pre-shock structures (see also figure 12). This process in conjunction with a vorticity deposition that is one order of magnitude larger than the pre-shock deposition leads to rapid formation of complex disordered structures, which eliminates most of the memory of the initial interface perturbation, as can be seen in figures 12–14. Schilling, Latini & Don (2007) reported that during re-shock vorticity production is strongly enhanced along the interface where density gradients and misalignment of pressure and density gradients is largest. The vorticity deposited by the re-shock transforms bubbles into spikes and vice versa, which subsequently results in more complex and highly disordered structures.
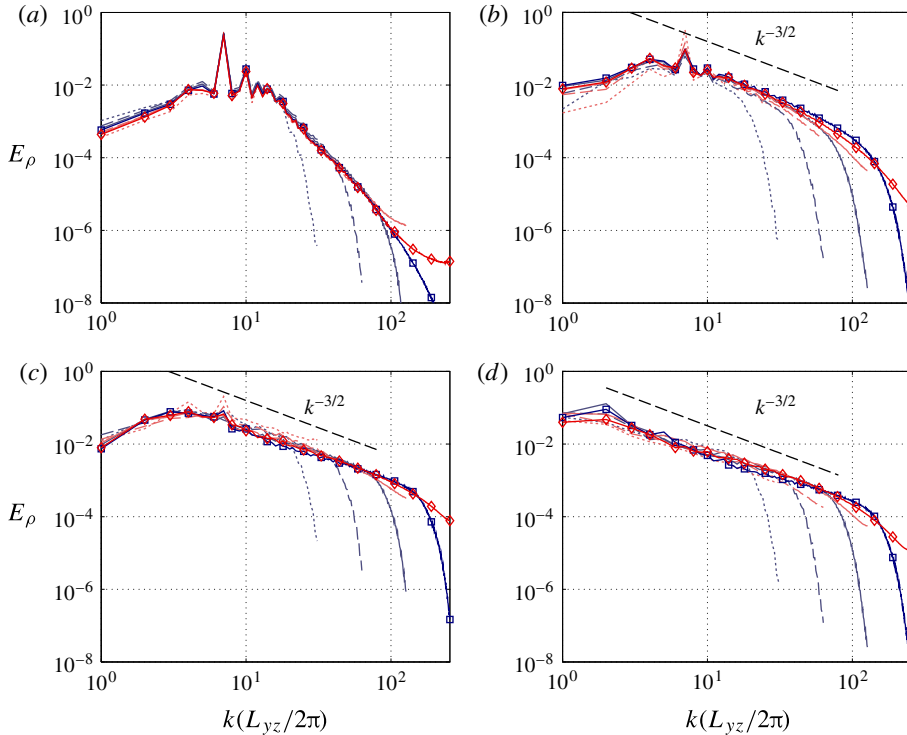
FIGURE 13. (Colour online) Power spectra of density from Miranda (dark grey; blue online) and INCA (light grey; red online) before re-shock at (*a*) $t = 0.5$ ms and (*b*) $t = 2$ ms and after re-shock at (*c*) $t = 2.5$ ms and (*d*) $t = 6$ ms. The different resolutions are represented as dotted line (64), dashed line (128), solid line (256) and solid line with open squares for Miranda and open diamonds for INCA (512).

At late times the power spectra of density appear to be more shallow than $k^{-3/2}$, and rather approach $k^{-6/5}$, as was found by Cohen *et al.* (2002). The smallest length scale in scalar turbulence is the Batchelor scale. For isotropic turbulence and Schmidt numbers of order unity, it has the same order of magnitude as the Kolmogorov microscale $\lambda_B \approx \eta$. Therefore, the TKE spectra are closely correlated with the scalar power spectra. Figure 14 shows the spectra of TKE before and after re-shock. The significant increase in TKE is mainly due to the interaction of the enhanced small-scale structures with comparatively steep density gradients and the reflected shock wave. The re-shock at $t \approx 2$ ms leads to a self-similar lifting of the spectrum (see figure 14). The destruction process of the vortical structures initiated by the re-shock leads to the formation of small scales, which rapidly remove the memory of the initial condition. The intense fluctuating velocity gradients past re-shock are rapidly smoothed out by viscous stresses. This results in a fast decay of the TKE following the first ≈ 0.5 ms after re-shock (see figures 8 and 14*c*,*d*).

The sharp drop-off of the spectral energy in figures 13 and 14 in the Miranda data at high wavenumbers is due to the filtering operator of the numerical method. Opposite behaviour, that is, an increase of spectral energy at the highest wavenumbers, is observed for the less dissipative INCA code, where the spurious behaviour at the non-resolved scales is mainly dispersive.
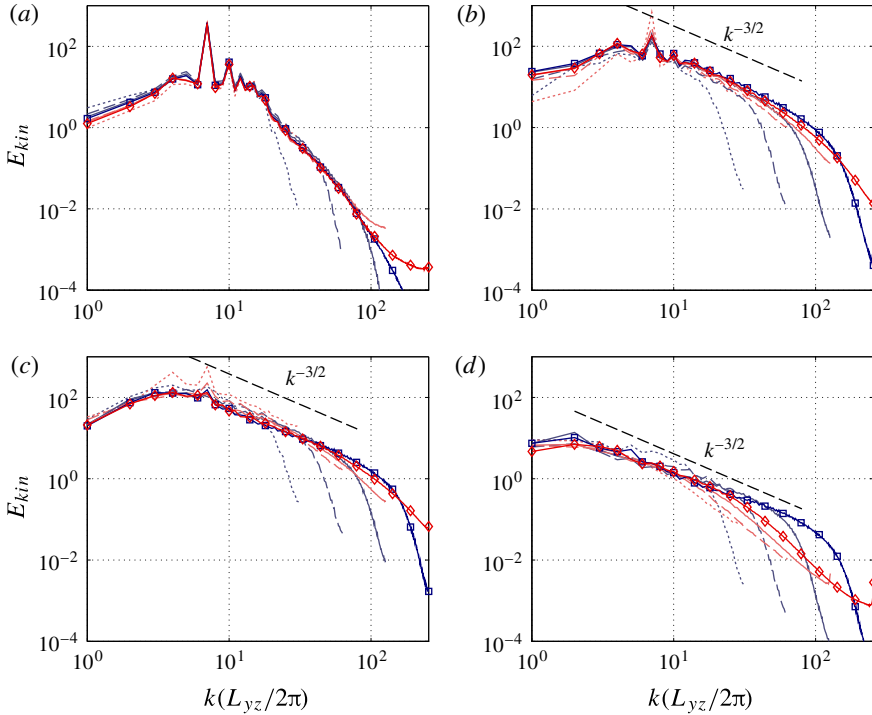
FIGURE 14. (Colour online) Spectra of TKE from Miranda (dark grey; blue online) and INCA (light grey; red online) before re-shock at (*a*) $t = 0.5$ ms and (*b*) $t = 2$ ms and after re-shock at (*c*) $t = 2.5$ ms and (*d*) $t = 6$ ms. The different resolutions are represented as dotted line (64), dashed line (128), solid line (256) and solid line with open squares for Miranda and open diamonds for INCA (512).

The scaled TKE spectra $kE_{kin}(k)$ represent the effective energy contributed by each mode. Artifacts of the initial conditions still exist immediately before re-shock at $t = 2.0$ ms, as can be seen in figure 15(*a*), where most energy is contained at mode $k(L_{yz}/2\pi) = 7$. At re-shock, baroclinic vorticity is deposited at the interface and the energy-containing wavenumber range immediately widens as vortex stretching and tangling introduce new scales and higher vorticity. This broader profile is plotted in figure 15(*b*), which clearly shows that the relative difference between the imposed initial length scale $k(L_{yz}/2\pi) = 7$ and the remaining length scales (both larger and smaller) is vanishing. Indeed, as the mixing layer fully transitions to turbulence, the flow reaches a self-similar state where the memory of initial perturbations is lost.

The spectra of the scalar dissipation rate χ in figure 16 quickly build up in the cut-off wavenumber range after the initial shock impact (see figure 16*b*). After re-shock and at late time (see figure 16*c,d*), the inertial subrange broadens to wavenumbers where numerical dissipation damps out structures. The inertial range is observed to scale with $k^{1/2}$ after re-shock, which is consistent with the $k^{-3/2}$ scaling observed for E_ρ and E_{kin}. For the resolved wavenumbers, there is good agreement between both codes at the finest two resolutions. Differences observed in figure 16(*b*) are also reflected in figures 7 and 11. A sharper material interface and the associated segregation of the fluids lead to a higher scalar dissipation rate (χ), whereas at late
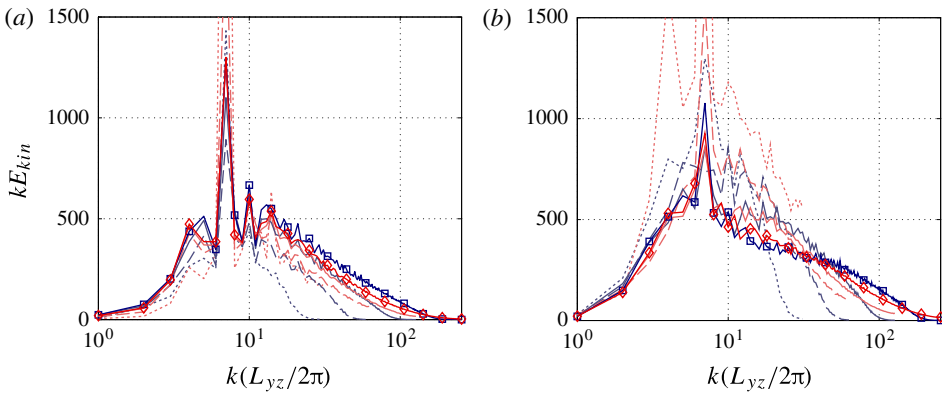
FIGURE 15. (Colour online) Scaled spectra of TKE from Miranda (dark grey; blue online) and INCA (light grey; red online) before re-shock at (*a*) $t = 2$ ms and (*b*) $t = 2.5$ ms. The different resolutions are represented as dotted line (64), dashed line (128), solid line (256) and solid line with open squares for Miranda and open diamonds for INCA (512).
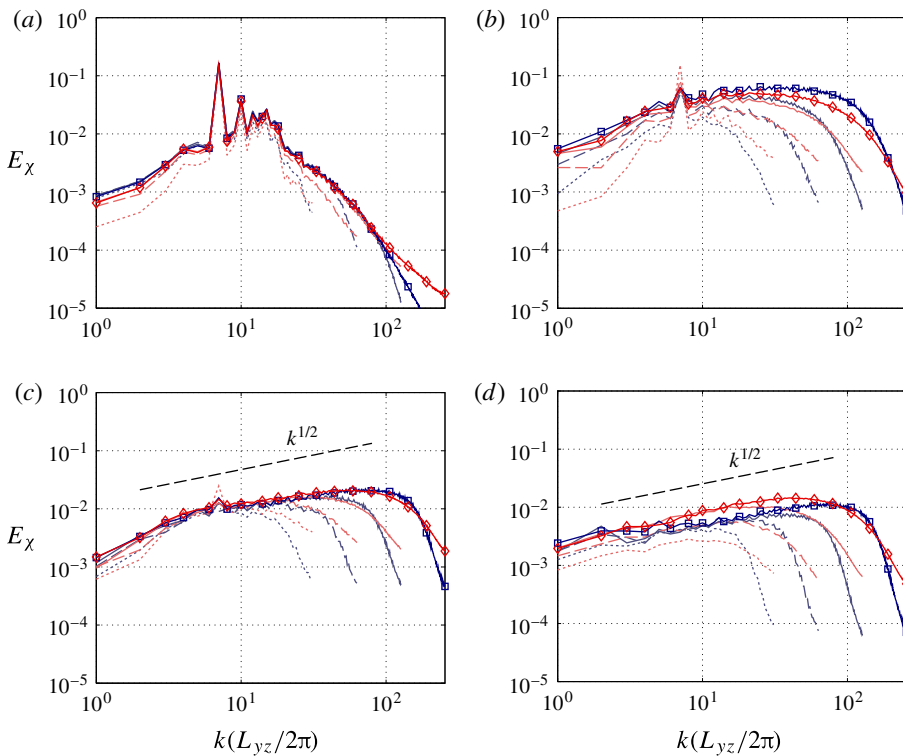

FIGURE 16. (Colour online) Spectra of scalar dissipation rate from Miranda (dark grey; blue online) and INCA (light grey; red online) before re-shock at (*a*) $t = 0.5$ ms and (*b*) $t = 2$ ms and after re-shock at (*c*) $t = 2.5$ ms and (*d*) $t = 6$ ms. The different resolutions are represented as dotted line (64), dashed line (128), solid line (256) and solid line with open squares for Miranda and open diamonds for INCA (512).

FIGURE 17. (Colour online) Spectra of enstrophy from Miranda (dark grey; blue online) and INCA (light grey; red online) before re-shock at (a) $t = 0.5$ ms and (b) $t = 2$ ms and after re-shock at (c) $t = 2.5$ ms and (d) $t = 6$ ms. The different resolutions are represented as dotted line (64), dashed line (128), solid line (256) and solid line with open squares for Miranda and open diamonds for INCA (512).
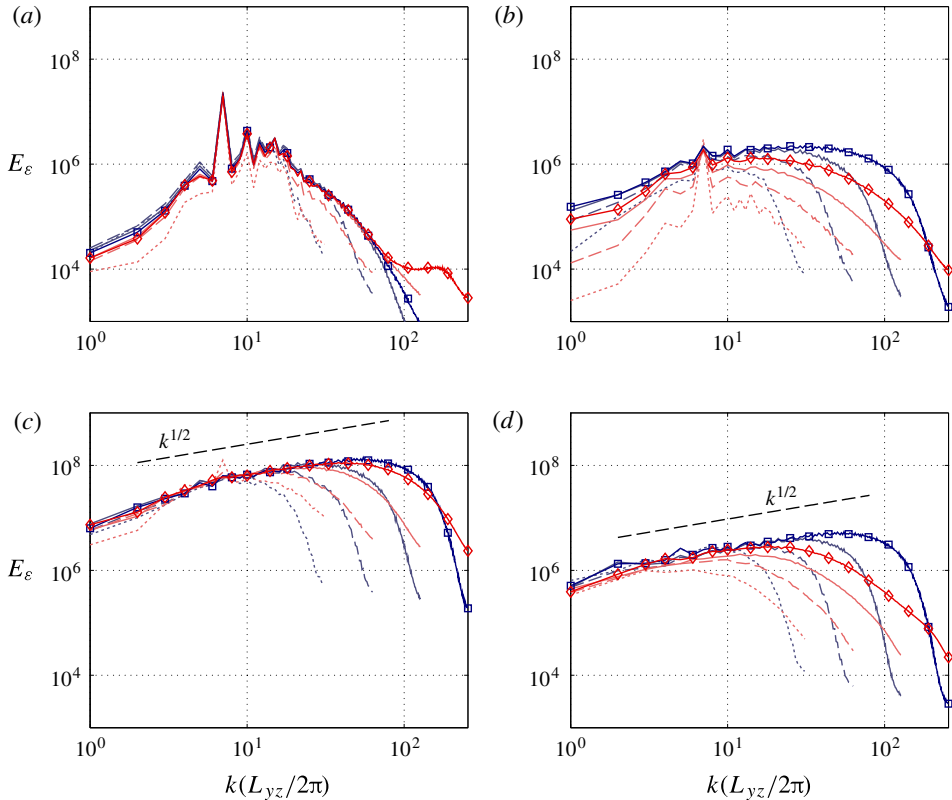
times the difference in the scalar dissipation rate does not significantly influence the mixing measures $\langle b \rangle_{xyz}$ and Θ.

Larger quantitative differences are observed in the power spectra of enstrophy shown in figure 17. Immediately after either of the shock–interface interactions, the quantitative agreement between the predicted enstrophy levels is excellent (see figure 17a,c). The observed scalings of the inertial range following re-shock are predicted consistently and agree with the inertial range scalings for the scalar dissipation rate $k^{1/2}$. However, the temporal decay of the small-scale enstrophy is significantly different for either code, as can be seen immediately before re-shock and long after re-shock in figures 17(b) and (d), respectively.

In isotropic homogeneous turbulence, the scaled spectra of the enstrophy (see figure 18) has a single peak at the wavenumber where the dissipation range begins. Therefore, under grid refinement this peak will shift to higher wavenumbers and magnitudes as smaller scales are captured. The peak at $k(L_{yz}/2\pi) = 7$ is associated with the initial perturbation and disappears after re-shock as the flow becomes turbulent (see figure 18). Good agreement for lower wavenumbers is observed between codes and resolutions. Larger differences are observed at high wavenumbers, where
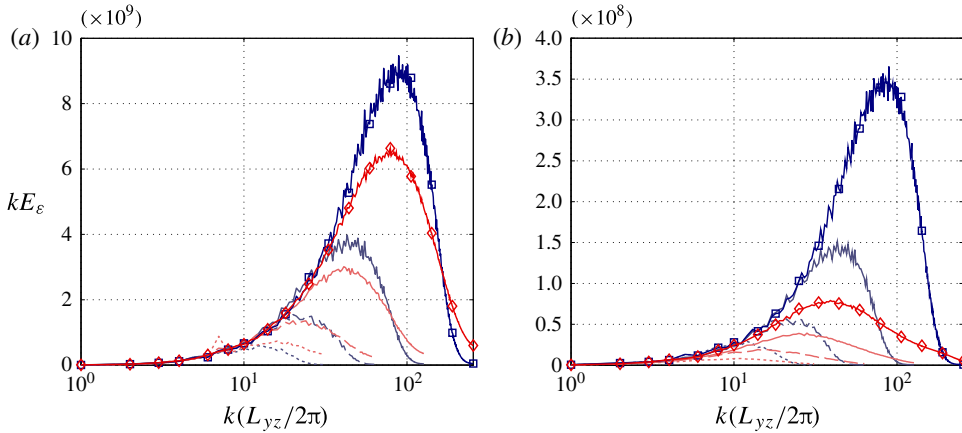
FIGURE 18. (Colour online) Scaled spectra of enstrophy from Miranda (dark grey; blue online) and INCA (light grey; red online) after re-shock at (*a*) $t = 2.5$ ms and (*b*) $t = 6$ ms. The different resolutions are represented as dotted line (64), dashed line (128), solid line (256) and solid line with open squares for Miranda and open diamonds for INCA (512).

the dependence on numerical dissipation is greatest. At $t = 2.5$ ms the peak in the scaled enstrophy spectra is at $k(L_{yz}/2\pi) \approx 85$ for both codes at the highest resolution. Later, at $t = 6.0$ ms this peak has shifted to $k(L_{yz}/2\pi) \approx 40$ in INCA, whereas in Miranda there is no apparent shift, although both have substantially decayed in magnitude.

As RMI is a pure decay process after re-shock, differences in the numerical approach become most apparent at late times. The numerical models of this study predict different turbulence decay rates, as is evident from differences in the enstrophy spectrum (figures 17 and 18) and in TKE (figure 9). The differences in enstrophy (ε) and scalar dissipation rate (χ) have a qualitative effect that becomes apparent in the fine-scale structures of figure 5 at $t = 6$ ms. Although INCA resolved less scales with smaller enstrophy levels, it does resolve steeper mass fraction gradients, which is reflected in the higher χ and higher levels of E_χ. Although it is unclear which dissipation rate (scalar or kinetic) has most effect on the mixing process, both are important (Dimotakis 2000).

4.4. *Probability density functions*

The bin size for computing the discrete probability density function (p.d.f.) is defined as $\Delta\varphi = [\varphi_{max} - \varphi_{min}]/N_b$ for a quantity $\varphi(x, y, z, t)$. The number of bins for all quantities and all grid resolutions is $N_b = 64$. Each discrete value of φ is distributed into the bins, yielding a frequency N_k for each bin. The p.d.f. is then defined by

$$P_k(\varphi, t) = \frac{N_k}{\Delta\varphi N}, \tag{4.13}$$

such that $\sum_{k=1}^{N_k} P_k \Delta\varphi = 1$, with N as the total number of cells in the IMZ that fall within the range $\varphi_{min} \leqslant \varphi \leqslant \varphi_{max}$. The limits φ_{max} and φ_{min} are held constant for all resolutions and times.

The p.d.f. of the heavy-gas mass fraction is constrained to be $0.1 \leqslant Y_{HG} \leqslant 0.9$. Figure 19 shows the p.d.f. at times before re-shock ($t = 0.5$ ms, $t = 2$ ms) and
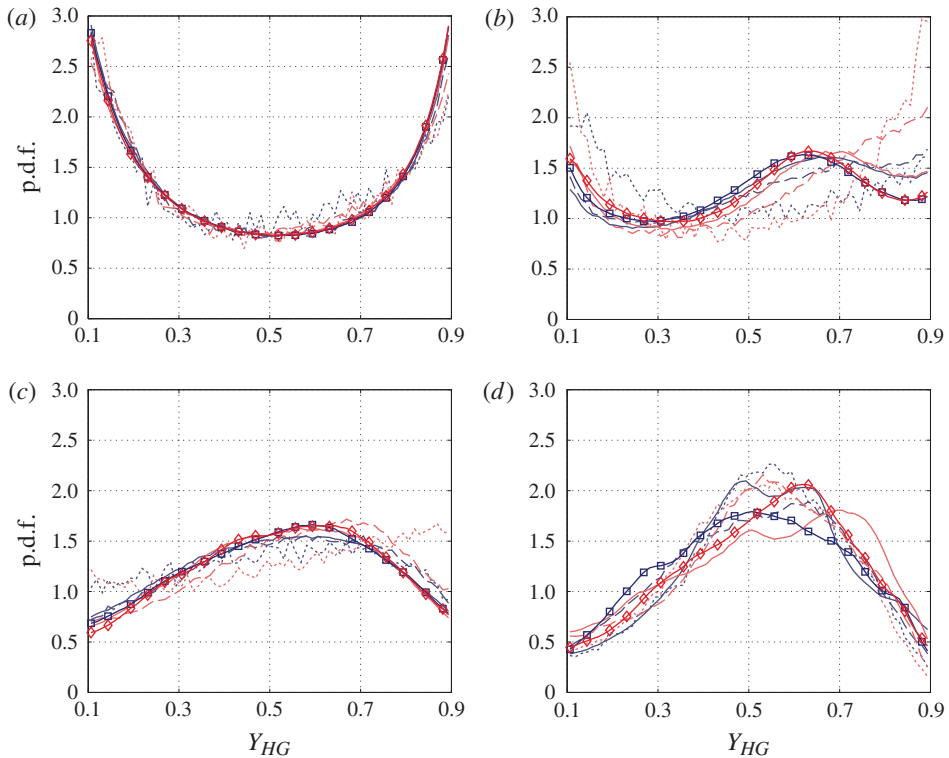
FIGURE 19. (Colour online) Probability density function of Y_{HG} from Miranda (dark grey; blue online) and INCA (light grey; red online) before re-shock at (*a*) $t = 0.5$ ms and (*b*) $t = 2$ ms and after re-shock at (*c*) $t = 2.5$ ms and (*d*) $t = 6$ ms. The different resolutions are represented as dotted line (64), dashed line (128), solid line (256) and solid line with open squares for Miranda and open diamonds for INCA (512).

following re-shock ($t = 2.5$ ms, $t = 6$ ms). From figure 19(*a*) it is evident that at early times following the initial shock–interface interaction the IMZ consists mostly of segregated fluid, as the large peaks at the p.d.f. bounds indicate. Before re-shock, inter-species mixing is largely dominated by the inviscid linear and nonlinear entrainment. Molecular diffusion processes have not yet had enough time to act (see figure 19*b*). Following re-shock, a fundamental change in the p.d.f. of Y_{HG} ($P(Y_{HG})$) is observed (see figure 19*c*,*d*). The additional vorticity deposited by the re-shock leads to rapid formation of small and very intense vortical structures that lead to very effective mixing and destruction of the initial interface perturbation. The p.d.f. takes a unimodal form at $t = 2.5$ ms, as also reported by Hill *et al.* (2006). The peak value, however, is not as well correlated with the average value of the mixture mass fraction as was reported by Hill *et al.* (2006). With our data the peak value is slightly shifted towards the heavy-gas side centred around $Y_{HG} \approx 0.6$. The degree of convergence between codes and resolutions is reassuring at $t = 2.5$ ms. Note that $P(Y_{HG})$ is a very sensitive measure of the light–heavy gas mixing.

The rarefaction wave at $t \approx 3.2$ ms does not significantly contribute to the mixing, as it is not as pronounced as found in comparable investigations (Hill *et al.* 2006; Grinstein *et al.* 2011). Long after re-shock the mixing process continues, which is reflected in narrower tails of $P(Y_{HG})$. The peak value of Y_{HG} predicted by Miranda now
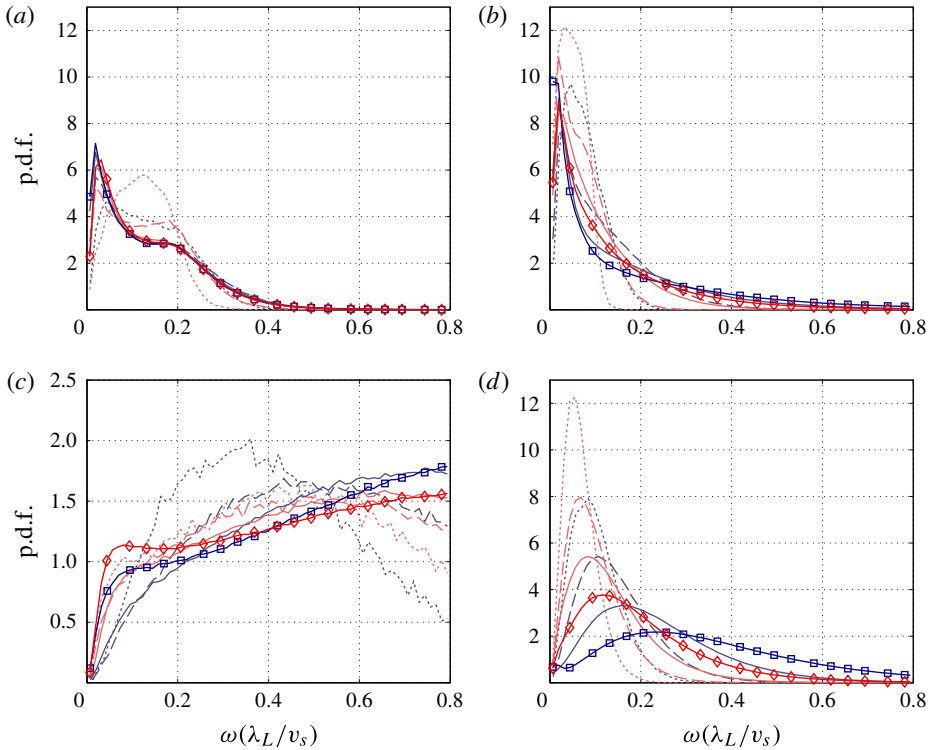
FIGURE 20. (Colour online) Probability density function of $\omega(\lambda_L/v_s)$ from Miranda (dark grey; blue online) and INCA (light grey; red online) before re-shock at (*a*) $t = 0.5$ ms and (*b*) $t = 2$ ms and after re-shock at (*c*) $t = 2.5$ ms and (*d*) $t = 6$ ms. The different resolutions are represented as dotted line (64), dashed line (128), solid line (256) and solid line with open squares for Miranda and open diamonds for INCA (512).

coincides with the average value of the mixture mass fraction. In the INCA results, this value remains slightly shifted towards the heavy-gas side. However, the bimodal character of $P(Y_{HG})$ reported by Hill *et al.* (2006), who used air–SF$_6$ as light–heavy gases, is not observed on the finest grid. Despite the strong mixing past re-shock the turbulent mixing zone remains inhomogeneous until the end of the simulation time, which makes the observed p.d.f. very sensitive to their location of evaluation within the mixing layer.

The p.d.f. of the normalised vorticity is constrained between $0 \leqslant \tilde{\omega} \leqslant 0.8$ with $\tilde{\omega} = \omega(\lambda_L/v_s)$, where v_s is the initial shock velocity and λ_L is a characteristic length scale of the perturbations taken as $\lambda_L = L_{yz}/\tilde{k}_{max}$, where L_{yz} is the width of the domain in the transverse direction and $\tilde{k}_{max} = k_{max}(L_{yz}/2\pi) = 16$.

Figure 20 shows the p.d.f. of the normalised vorticity $P(\tilde{\omega})$. Before re-shock, mixing is driven by weak large-scale vortices (see figure 20*a,b*). Following re-shock, however, structures with very intense vorticity develop with a dual-mode shape in $P(\tilde{\omega})$ at $t = 2.5$ ms on the finest grid. The early times after the second shock–interface interaction are again consistently predicted by both codes (figure 20*c*). Nevertheless, we observe larger differences for $P(\tilde{\omega})$ at $t = 6$ ms. The peak and distribution of $P(\tilde{\omega})$ from Miranda are shifted towards larger values of $\tilde{\omega}$ as compared to INCA. This supports the previous observation that the vorticity decay is affected by the numerical

approach. The difference in the vorticity intensity observed in figure 20, however, does not lead to noticeable differences for the integral mixing measures shown in figures 7(*a*) and 11 or for the integral length scale in figure 6.

5. Conclusion

We have investigated the shock-induced turbulent mixing between a light (N_2, O_2) and heavy (SF_6, acetone) gas in highly resolved numerical simulations. The mixing was initiated by the interaction of a $Ma = 1.5$ shock wave with a deterministic multimode interface. After the initial baroclinic vorticity deposition, the shock wave is reflected at the opposite adiabatic wall boundary. The reflected shock wave impacts the interface (re-shock) and deposits additional vorticity with enstrophy that is more than two orders of magnitude larger than that of the initial vorticity deposition. The transformation of spike structures into bubbles and vice versa in conjunction with a large increase in vorticity results in the formation of disordered structures which eliminate most of the memory of the initial interface perturbation.

A proposed standardised initial condition for simulating the RMI has been assessed by two different numerical approaches, Miranda and INCA, over a range of grid resolutions. The deterministic interface definition allows for spectrally identical initial conditions for different numerical models and grid resolutions. A direct comparison shows that larger energy-containing scales are in excellent agreement. Different subgrid-scale regularisations affect marginally resolved flow scales, but allow for a clear identification of a resolved scale range that is unaffected by the subgrid-scale regularisation.

Mixing widths are nearly identical between the two approaches at the highest resolution. At lower resolutions, the solutions differ, and we found a minimum resolution of $\sim$400 µm to be necessary in order to produce reasonable late-time results. The initial mixing zone growth rate scaled with $\delta_x \sim t^{7/12}$, whereas long after re-shock the predicted growth rate was $\sim t^{2/7}$. The decay of TKE was also found to be consistent and in good agreement between the approaches. The decay scaled with TKE $\sim t^{-10/7}$ at late times, which corresponds to a growth-rate scaling of the energy-containing eddies of $\sim t^{2/7}$. The agreement in the large scales of the solution between the two approaches is striking and has not been observed before.

Previous work on three-dimensional LES of RMI has examined numerical dependence only indirectly. For example, Thornber *et al.* (2010) performed a code comparison of single-shock RMI. However, the initialisation was different for the two codes and the purpose was not to quantify the effect of different numerical methods. Accordingly, the comparison of results at different resolutions for mean, spectral and gradient-based quantities was limited. With the current work, we have presented for the first time a comprehensive quantitative analysis of numerical effects on RMI.

Our results conclusively show that the large scales are in excellent agreement for the two methods. Differences are observed in the representation of the material interface. We conclude that the numerical challenge, prior to re-shock, is to predict the large-scale nonlinear entrainment and the associated interface sharpening. Under shear and strain, the interface steepens and eventually becomes under-resolved with a thickness defined by the resolution limit of the numerical scheme. Therefore, the saturation of the interface thickness by the numerical method occurs later as the grid is refined. The molecular mixing fraction reached an asymptotic limit as $\Theta \approx 0.85$ after re-shock, which was already correctly calculated on grid resolutions of $\sim$400 µm. The yz plane averaged anisotropy $\langle a \rangle_{yz}$ revealed that the mixing zone

exhibits a stratified anisotropy distribution with lower anisotropy on the heavy-gas side and higher anisotropy on the light-gas side. Moreover, the volume-averaged anisotropy $\langle a \rangle_{xyz}$ approached an asymptotic limit of $\langle a \rangle_{xyz} \approx 0.04$, implying that the fluctuating velocity component u'' remains the dominant component even after re-shock and that no full recovery of isotropy of the mixing zone is obtained. The density self-correlation has been investigated in order to better understand the mixing inhomogeneity in the mixing zone. The volume-averaged density-specific volume correlation $\langle b \rangle_{xyz}$ showed that the re-shock significantly increases mixing homogeneity approaching a value of $\langle b \rangle_{xyz} \approx 0.13$ at the latest time.

The spectra demonstrate a broad range of resolved scales, which are in very good agreement. Data also show that differences exist in the small-scale range. The frequency dependence of the velocity and density fluctuations shows the existence of an inertial subrange and that the two approaches agree at lower frequencies. The observed spectral scalings were consistent among the methods with $k^{-3/2}$.

Quantities that are gradient-dependent and therefore more sensitive to small scales, such as the scalar dissipation rate and enstrophy, exhibit stronger dependence on numerical method and grid resolution. The flow field shows visual differences for the fine-scale structures at late times. The tenth-order compact scheme and the explicit filtering and artificial fluid properties used in Miranda resolved more small scales in TKE and enstrophy, whereas the sixth-order WENO-based scheme used in INCA resolves more of the small-scale scalar flow features as observed in the spectra of density and scalar dissipation rate. This result is somewhat intuitive given the numerics of the two codes. High-order compact methods are capable of resolving higher modes than explicit finite difference methods (Lele 1992). Given that the artificial shear viscosity in Miranda has only a small effect on the solution compared to the effect of the eighth-order filter, the primary difference, we conclude, of the resolving power between methods is due to the difference in order of accuracy and modified wavenumber profiles between the schemes. The compact finite difference method with high-order filtering appears to capture a broader range of dynamic scales at late times.

The p.d.f. statistics of heavy-gas mass fraction Y_{HG} revealed that the IMZ remains inhomogeneous until the end of the simulation and that the peak probability is centred around $Y_{HG} \approx 0.6$ and thus is slightly shifted towards the heavy-gas side. Although the overall quantitative agreement was very good, the p.d.f. of the vorticity showed larger differences once intense small-scale vortical structures exist. The decay of vorticity differs accordingly between the numerical methods.

Acknowledgements

Appendix A. Multicomponent mixing rules

The specific heat capacity of species i is found by

$$c_{p,i} = \frac{\gamma_i}{\gamma_i - 1} R_i, \quad \text{with } R_i = \frac{R_{univ}}{M_i}, \tag{A 1}$$

where γ_i is the ratio of specific heats. The ratio of specific heats of the mixture follows as

$$\bar{\gamma} = \frac{\overline{c_p}}{\overline{c_p} - \bar{R}}, \quad \text{with} \quad \overline{c_p} = \sum_i^N Y_i c_{p,i}, \tag{A 2}$$

where Y_i is the mass fraction of species i and $\bar{R}$ is the specific gas constant of the mixture with $\bar{R} = R_{univ}/\bar{M}$. The molar mass of the mixture is given by

$$\bar{M} = \left(\sum_i^N \frac{Y_i}{M_i} \right)^{-1}. \tag{A 3}$$

For the gas mixture, Dalton's law $p = \sum_i p_i$ will be valid with $p_i = \rho R_i T$. The mixture viscosity $\bar{\mu}$ and the mixture thermal conductivity $\bar{\kappa}$ are calculated from (Reid, Pransuitz & Poling 1987)

$$\bar{\mu} = \frac{\displaystyle\sum_{i=1}^N \mu_i Y_i/M_i^{1/2}}{\displaystyle\sum_{i=1}^N Y_i/M_i^{1/2}}, \quad \bar{\kappa} = \frac{\displaystyle\sum_{i=1}^N \kappa_i Y_i/M_i^{1/2}}{\displaystyle\sum_{i=1}^N Y_i/M_i^{1/2}}. \tag{A 4a,b}$$

The effective binary diffusion coefficients (diffusion of species i into all other species) are approximated as (Ramshaw 1990)

$$D_i = (1 - X_i) \left(\sum_{i \neq j}^N \frac{X_j}{D_{ij}} \right)^{-1}, \tag{A 5}$$

where X_i is the mole fraction of species i. Equation (A 5) ensures that the inter-species diffusion fluxes balance to zero.

Appendix B. Molecular mixing rules

The viscosity of a pure gas is calculated from the Chapman–Enskog model (Chapman & Cowling 1990)

$$\mu_i = 2.6693 \times 10^{-6} \frac{\sqrt{M_i T}}{\Omega_{\mu,i} \sigma_i^2}, \tag{B 1}$$

where σ_i is the collision diameter and $\Omega_{\mu,i}$ is the collision integral,

$$\Omega_{\mu,i} = A(T_i^*)^B + C \exp(D T_i^*) + E \exp(F T_i^*), \tag{B 2}$$

with $A = 1.16145$, $B = -0.14874$, $C = 0.52487$, $D = -0.7732$, $E = 2.16178$ and $F = -2.43787$ and where $T_i^* = T/(\epsilon/k)_i$. Here $(\epsilon/k)_i$ is the Lennard-Jones energy parameter, with ϵ the minimum of the Lennard-Jones potential and k the Boltzmann constant.

The thermal conductivity of species i is defined by

$$\kappa_i = c_{p,i} \frac{\mu_i}{Pr_i}, \tag{B 3}$$

with Pr_i the species-specific Prandtl number.

Property	Nitrogen	Oxygen	SF$_6$	Acetone
$(\epsilon/k)_i$ (K)	82.0	102.6	212.0	458.0
σ_i (Å)	3.738	3.48	5.199	4.599
M_i (g mol^{-1})	28.0140	31.9990	146.0570	58.0805
γ_i	1.4	1.4	1.1	1.1
Pr_i	0.72	0.72	0.8	0.8

TABLE 2. Molecular properties of nitrogen, oxygen, SF$_6$ and acetone.

The mass diffusion coefficient of a binary mixture is calculated from the empirical law (Reid *et al.* 1987)

$$D_{ij} = \frac{0.0266}{\Omega_{D,ij}} \frac{T^{3/2}}{p\sqrt{M_{ij}}\sigma_{ij}^2}, \tag{B 4}$$

with the collision integral for diffusion

$$\Omega_{D,ij} = A(T_{ij}^*)^B + C\exp(DT_{ij}^*) + E\exp(FT_{ij}^*) + G\exp(HT_{ij}^*), \tag{B 5}$$

where $T_{ij}^* = T/T_{\epsilon_{ij}}$ and $A = 1.060\,36$, $B = -0.1561$, $C = 0.193\,00$, $D = -0.476\,35$, $E = 1.035\,87$, $F = -1.529\,96$, $G = 1.764\,74$, $H = -3.894\,11$ and

$$M_{ij} = \frac{2}{\dfrac{1}{M_i} + \dfrac{1}{M_j}}, \tag{B 6a}$$

$$\sigma_{ij} = \frac{\sigma_i + \sigma_j}{2}, \tag{B 6b}$$

$$T_{\epsilon_{ij}} = \sqrt{\left(\frac{\epsilon}{k}\right)_i \left(\frac{\epsilon}{k}\right)_j}. \tag{B 6c}$$

The molecular properties of all species in the present study are given in table 2.

REFERENCES

AGLITSKIY, Y., VELIKOVICH, A. L., KARASIK, M., METZLER, N., ZALESAK, S. T., SCHMITT, A. J., PHILLIPS, L., GARDNER, J. H., SERLIN, V., WEAVER, J. L. & OBENSCHAIN, S. P. 2010 Basic hydrodynamics of Richtmyer–Meshkov-type growth and oscillations in the inertial confinement fusion-relevant conditions. *Phil. Trans. R. Soc. Lond.* A **368** (1916), 1739–1768.

ALMGREN, A. S., BELL, J. B., RENDLEMAN, C. A. & ZINGALE, M. 2006 Low Mach number modeling of type Ia supernovae I. Hydrodynamics. *Astrophys. J.* **637**, 922–936.

ARNETT, D. 2000 The role of mixing in astrophysics. *Astrophys. J. Suppl.* **127**, 213–217.

ARNETT, W. D., BAHCALL, J. N., KIRSHNER, R. P. & STANFORD, E. W. 1989 Supernova 1987a. *Annu. Rev. Astron. Astrophys.* **27**, 629–700.

BALAKUMAR, B. J., ORLICZ, G. C., RISTORCELLI, J. R., BALASUBRAMANIAN, S., PRESTRIDGE, K. P. & TOMKINS, C. D. 2012 Turbulent mixing in a Richtmyer–Meshkov fluid layer after reshock: velocity and density statistics. *J. Fluid Mech.* **696**, 67–93.

BALASUBRAMANIAN, S., ORLICZ, G. C. & PRESTRIDGE, K. P. 2013 Experimental study of initial condition dependence on turbulent mixing in shock-accelerated Richtmyer–Meshkov fluid layers. *J. Turbul.* **14** (3), 170–196.

BALASUBRAMANIAN, S., ORLICZ, G. C., PRESTRIDGE, K. P. & BALAKUMAR, B. J. 2012 Experimental study of initial condition dependence on Richtmyer–Meshkov instability in the presence of reshock. *Phys. Fluids* **24**, 034103.

BATCHELOR, G. K. & PROUDMAN, I. 1956 The large-scale structure of homogeneous turbulence. *Phil. Trans. R. Soc. Lond.* A **248**, 369–405.

BESNARD, D., HARLOW, F. H., RAUENZAHN, R. M. & ZEMACH, C. 1992 Turbulence transport equations for variable-density turbulence and their relationship to two-field models. *Recon Tech. Rep.* No. 92, 33159. NASA STI.

BROUILLETTE, M. 2002 The Richtmyer–Meshkov instability. *Annu. Rev. Fluid Mech.* **34**, 445–468.

CABOT, W. H. & COOK, A. W. 2006 Reynolds number effects on Rayleigh–Taylor instability with possible implications for type Ia supernovae. *Nat. Phys.* **2** (8), 562–568.

CHAPMAN, S. & COWLING, T. G. 1990 *The Mathematical Theory of Non-Uniform Gases: An Account of the Kinetic Theory of Viscosity*. Cambridge University Press.

COHEN, R. H., DANNEVIK, W. P., DIMITS, A. M., ELIASON, D. E., MIRIN, A. A., ZHOU, Y., PORTER, D. H. & WOODWARD, P. R. 2002 Three-dimensional simulation of a Richtmyer–Meshkov instability with a two-scale initial perturbation. *Phys. Fluids* **14** (10), 3692–3709.

COOK, A. W. 2007 Artificial fluid properties for large-eddy simulation of compressible turbulent mixing. *Phys. Fluids* **19** (5), 055103.

COOK, A. W. 2009 Enthalpy diffusion in multicomponent flows. *Phys. Fluids* **21**, 055109.

COOK, A. W., CABOT, W. & MILLER, P. L. 2004 The mixing transition in Rayleigh–Taylor instability. *J. Fluid Mech.* **511**, 333–362.

DIMONTE, G., FRERKING, C. E. & SCHNEIDER, M. 1995 Richtmyer–Meshkov instability in the turbulent regime. *Phys. Rev. Lett.* **74**, 4855–4858.

DIMONTE, G. & SCHNEIDER, M. 2000 Density ratio dependence of Rayleigh–Taylor mixing for sustained and impulsive acceleration histories. *Phys. Fluids* **12** (2), 304–321.

DIMOTAKIS, P. E. 2000 The mixing transition in turbulent flows. *J. Fluid Mech.* **409**, 69–98.

DRIKAKIS, D. 2003 Advances in turbulent flow computations using high-resolution methods. *Prog. Aerosp. Sci.* **39** (6–7), 405–424.

DRIKAKIS, D., HAHN, M., MOSEDALE, A. & THORNBER, B. 2009 Large eddy simulation using high-resolution and high-order methods. *Phil. Trans. R. Soc. Lond.* A **367** (1899), 2985–2997.

FEDKIW, R. P., MERRIMAN, B. & OSHER, S. 1997 High accuracy numerical methods for thermally perfect gas flows with chemistry. *J. Comput. Phys.* **190**, 175–190.

GOTTLIEB, S. & SHU, C.-W. 1998 Total variation diminishing Runge–Kutta schemes. *Math. Comput.* **67**, 73.

GRINSTEIN, F. F., GOWARDHAN, A. A. & WACHTOR, A. J. 2011 Simulations of Richtmyer–Meshkov instabilities in planar shock-tube experiments. *Phys. Fluids* **23**, 034106.

HAHN, M., DRIKAKIS, D., YOUNGS, D. L. & WILLIAMS, R. J. R. 2011 Richtmyer–Meshkov turbulent mixing arising from an inclined material interface with realistic surface perturbations and reshocked flow. *Phys. Fluids* **23** (4), 046101.

HILL, D. J., PANTANO, C. & PULLIN, D. I. 2006 Large-eddy simulation and multiscale modelling of a Richtmyer–Meshkov instability with reshock. *J. Fluid Mech.* **557**, 29–61.

HILL, D. J. & PULLIN, D. I. 2004 Hybrid tuned center-difference-WENO method for large eddy simulations in the presence of strong shocks. *J. Comput. Phys.* **194**, 435–450.

HU, X. Y. & ADAMS, N. A. 2011 Scale separation for implicit large eddy simulation. *J. Comput. Phys.* **230** (19), 7240–7249.

HU, X. Y., ADAMS, N. A. & SHU, C.-W. 2013 Positivity-preserving method for high-order conservative schemes solving compressible Euler equations. *J. Comput. Phys.* **242**, 169–180.

HU, X. Y., WANG, Q. & ADAMS, N. A. 2010 An adaptive central-upwind weighted essentially non-oscillatory scheme. *J. Comput. Phys.* **229** (23), 8952–8965.

ISHIDA, T., DAVIDSON, P. A. & KANEDA, Y. 2006 On the decay of isotropic turbulence. *J. Fluid Mech.* **564**, 455–475.

JIMÉNEZ, J., WRAY, A. A., SAFFMAN, P. G. & ROGALLO, R. S. 1993 The structure of intense vorticity in isotropic turbulence. *J. Fluid Mech.* **255**, 65–90.

KENNEDY, C. A., CARPENTER, M. H. & LEWIS, M. R. 2000 Low-storage, explicit Runge–Kutta schemes for the compressible Navier–Stokes equations. *Appl. Numer. Maths* **35** (3), 177–219.

KHOKHLOV, A. M., ORAN, E. S. & THOMAS, G. O. 1999 Numerical simulation of deflagration-to-detonation transition: the role of shock–flame interactions in turbulent flames. *Combust. Flame* **117** (1–2), 323–339.

KOLMOGOROV, A. N. 1941 On the degeneration of isotropic turbulence in an incompressible viscous fluid. *Dokl. Akad. Nauk SSSR* **31**, 538–541.

KOSOVIĆ, B., PULLIN, D. I. & SAMTANEY, R. 2002 Subgrid-scale modeling for large-eddy simulations of compressible turbulence. *Phys. Fluids* **14** (4), 1511–1522.

LAROUTUROU, B. & FEZOUI, L. 1989 On the equations of multi-component perfect or real gas inviscid flow. In *Nonlinear Hyperbolic Problems*, Lecture Notes in Mathematics, vol. 1402, pp. 69–97. Springer.

LELE, S. K. 1992 Compact finite-difference schemes with spectral-like resolution. *J. Comput. Phys.* **103**, 16–42.

LINDL, J. D., MCCRORY, R. L. & CAMPBELL, E. M. 1992 Progress toward ignition and burn propagation in inertial confinement fusion. *Phys. Today* **45** (9), 32–40.

LLOR, A. 2006 Invariants of free turbulent decay, arXiv:physics/0612220.

LOMBARDINI, M., HILL, D. J., PULLIN, D. I. & MEIRON, D. I. 2011 Atwood ratio dependence of Richtmyer–Meshkov flows under reshock conditions using large-eddy simulations. *J. Fluid Mech.* **670**, 439–480.

LOMBARDINI, M., PULLIN, D. I. & MEIRON, D. I. 2012 Transition to turbulence in shock-driven mixing: a Mach number study. *J. Fluid Mech.* **690**, 203–226.

MANI, A., LARSSON, J. & MOIN, P. 2009 Suitability of artificial bulk viscosity for large-eddy simulation of turbulent flows with shocks. *J. Comput. Phys.* **228** (19), 7368–7374.

MESHKOV, E. E. 1969 Instability of the interface of two gases accelerated by a shock wave. *Fluid Dyn.* **4**, 151–157.

MIKAELIAN, K. O. 1989 Turbulent mixing generated by Rayleigh–Taylor and Richtmyer–Meshkov instabilities. *Physica* D **36** (3), 343–357.

OLSON, B. J. & COOK, A. W. 2007 Rayleigh–Taylor shock waves. *Phys. Fluids* **19**, 128108.

OLSON, B. J., LARSSON, J., LELE, S. K. & COOK, A. W. 2011 Non-linear effects in the combined Rayleigh–Taylor/Kelvin–Helmholtz instability. *Phys. Fluids* **23**, 114107.

ORLICZ, G. C., BALASUBRAMANIAN, S. & PRESTRIDGE, K. P. 2013 Incident shock Mach number effects on Richtmyer–Meshkov mixing in a heavy gas layer. *Phys. Fluids* **25** (11), 114101.

PULLIN, D. I. 2000 A vortex-based model for the subgrid flux of a passive scalar. *Phys. Fluids* **12** (9), 2311–2319.

RAMSHAW, J. D. 1990 Self-consistent effective binary diffusion in multicomponent gas mixtures. *J. Non-Equilib. Thermodyn.* **15**, 295–300.

RAYLEIGH, LORD 1883 Investigation of the character of the equilibrium of an incompressible heavy fluid of variable density. *Proc. Lond. Math. Soc.* **14**, 170–177.

REID, R. C., PRANSUITZ, J. M. & POLING, B. E. 1987 *The Properties of Gases and Liquids*. McGraw-Hill.

RICHTMYER, R. D. 1960 Taylor instability in shock acceleration of compressible fluids. *Commun. Pure Appl. Maths* **13**, 297–319.

ROE, P. L. 1981 Approximate Riemann solvers, parameter and difference schemes. *J. Comput. Phys.* **43**, 357–372.

SAFFMAN, P. G. 1967a Note on decay of homogeneous turbulence. *Phys. Fluids* **10**, 1349.

SAFFMAN, P. G. 1967b The large-scale structure of homogeneous turbulence. *J. Fluid Mech.* **27**, 581–593.

SCHILLING, O. & LATINI, M. 2010 High-order WENO simulations of three-dimensional reshocked Richtmyer–Meshkov instability to late times: dynamics, dependence on initial conditions, and comparisons to experimental data. *Acta Math. Sci.* **30B**, 595–620.

SCHILLING, O., LATINI, M. & DON, W. S. 2007 Physics of reshock and mixing in single-mode Richtmyer–Meshkov instability. *Phys. Rev.* E **76**, 026319.

TACCETTI, J. M., BATHA, S. H., FINCKE, J. R., DELAMATER, N. D., LANIER, N. E., MAGELSSEN, G. R., HUECKSTAEDT, R. M., ROTHMAN, S. D., HORSFIELD, C. J. & PARKER, K. W. 2005 Richtmyer–Meshkov instability reshock experiments using laser-driven double-cylinder implosions. In *High Energy Density Laboratory Astrophysics* (ed. G. A. Kyrala), pp. 327–331. Springer.

TAYLOR, G. 1950 The instability of liquid surfaces when accelerated in a direction perpendicular to their planes. Part 1. Waves on fluid sheets. *Proc. R. Soc. Lond.* A **201**, 192–196.

THORNBER, B., DRIKAKIS, D., YOUNGS, D. L. & WILLIAMS, R. J. R. 2010 The influence of initial conditions on turbulent mixing due to Richtmyer–Meshkov instability. *J. Fluid Mech.* **654**, 99–139.

THORNBER, B., DRIKAKIS, D., YOUNGS, D. L. & WILLIAMS, R. J. R. 2011 Growth of a Richtmyer–Meshkov turbulent layer after reshock. *Phys. Fluids* **23**, 095107.

THORNBER, B., DRIKAKIS, D., YOUNGS, D. L. & WILLIAMS, R. J. R. 2012 Physics of the single-shocked and reshocked Richtmyer–Meshkov instability. *J. Turbul.* **13** (1), N10.

THORNBER, B., MOSEDALE, A., DRIKAKIS, D., YOUNGS, D. & WILLIAMS, R. J. R. 2008 An improved reconstruction method for compressible flows with low Mach number features. *J. Comput. Phys.* **227** (10), 4873–4894.

TOMKINS, C. D., BALAKUMAR, B. J., ORLICZ, G., PRESTRIDGE, K. P. & RISTORCELLI, J. R. 2013 Evolution of the density self-correlation in developing Richtmyer–Meshkov turbulence. *J. Fluid Mech.* **735**, 288–306.

TORO, E. F. 1999 *Riemann Solvers and Numerical Methods for Fluid Dynamics*. Springer.

TRITSCHLER, V. K., AVDONIN, A., HICKEL, S., HU, X. Y. & ADAMS, N. A. 2014 Quantification of initial-data uncertainty on a shock-accelerated gas cylinder. *Phys. Fluids* **26** (2), 026101.

TRITSCHLER, V. K., HICKEL, S., HU, X. Y. & ADAMS, N. A. 2013*a* On the Kolmogorov inertial subrange developing from Richtmyer–Meshkov instability. *Phys. Fluids* **25**, 071701.

TRITSCHLER, V. K., HU, X. Y., HICKEL, S. & ADAMS, N. A. 2013*b* Numerical simulation of a Richtmyer–Meshkov instability with an adaptive central-upwind 6th-order WENO scheme. *Phys. Scr.* **T155**, 014016.

WEBER, C. R., COOK, A. W. & BONAZZA, R. 2013 Growth rate of a shocked mixing layer with known initial perturbations. *J. Fluid Mech.* **725**, 372–401.

WEBER, C., HAEHN, N., OAKLEY, J., ROTHAMER, D. & BONAZZA, R. 2012 Turbulent mixing measurements in the Richtmyer–Meshkov instability. *Phys. Fluids* **24**, 074105.

WEBER, C. R., HAEHN, N. S., OAKLEY, J. G., ROTHAMER, D. A. & BONAZZA, R. 2014 An experimental investigation of the turbulent mixing transition in the Richtmyer–Meshkov instability. *J. Fluid Mech.* **748**, 457–487.

WILCZEK, M., DAITCHE, A. & FRIEDRICH, R. 2011 On the velocity distribution in homogeneous isotropic turbulence: correlations and deviations from gaussianity. *J. Fluid Mech.* **676**, 191–217.

YANG, J., KUBOTA, T. & ZUKOSKI, E. E. 1993 Applications of shock-induced mixing to supersonic combustion. *AIAA J.* **31**, 854–862.

YOUNGS, D. L. 1991 Three-dimensional numerical simulation of turbulent mixing by Rayleigh–Taylor instability. *Phys. Fluids* A: *Fluid Dyn.* **3** (5), 1312–1320.

YOUNGS, D. L. 1994 Numerical simulations of mixing by Rayleigh–Taylor and Richtmyer–Meshkov instabilities. *Laser Part. Beams* **12** (2), 538–544.

YOUNGS, D. L. 2004 Effect of initial conditions on self-similar turbulent mixing. In *Proceedings of the International Workshop on the Physics of Compressible Turbulent Mixing*, vol. 9.

YOUNGS, D. L. 2007 *Implicit Large Eddy Simulation: Computing Turbulent Fluid Dynamics*, pp. 392–412. Cambridge University Press.

ZABUSKY, N. J. 1999 Vortex paradigm for accelerated inhomogeneous flows: visiometrics for the Rayleigh–Taylor and Richtmyer–Meshkov environments. *Annu. Rev. Fluid Mech.* **31**, 495–536.

ZHOU, Y. 2001 A scaling analysis of turbulent flows driven by Rayleigh–Taylor and Richtmyer–Meshkov instabilities. *Phys. Fluids* **13** (2), 538–543.